Titre: Title:	Architecture of Integrated Battery-Less Sensor and Validation of its Critical Blocks
Auteur: Author:	Milad Salehi
Date:	2021
Type:	Mémoire ou thèse / Dissertation or Thesis
Référence: Citation:	Salehi, M. (2021). Architecture of Integrated Battery-Less Sensor and Validation of its Critical Blocks [Master's thesis, Polytechnique Montréal]. PolyPublie. https://publications.polymtl.ca/5621/

URL de PolyPublie: PolyPublie URL:	https://publications.polymtl.ca/5621/
Directeurs de recherche: Advisors:	Yvon Savaria, & Mohamad Sawan
Programme: Program:	génie électrique

POLYTECHNIQUE MONTRÉAL

affiliée à l'Université de Montréal

Architecture of integrated battery-less sensor and validation of its critical blocks

MILAD SALEHI

Département de génie électrique

Mémoire présenté en vue de l'obtention du diplôme de *Maîtrise ès sciences appliquées*

Génie électrique

Mars 2021

POLYTECHNIQUE MONTRÉAL

affiliée à l'Université de Montréal

Ce mémoire intitulé:

Architecture of integrated battery-less sensor and validation of its critical blocks

présenté par **Milad SALEHI**

en vue de l'obtention du diplôme de *Maîtrise ès sciences appliquées*

a été dûment accepté par le jury d'examen constitué de :

François LEDUC-PRIMEAU, président
Yvon SAVARIA, membre et directeur de recherche
Mohamad SAWAN, membre et codirecteur de recherche
Yves BLAQUIÈRE, membre

DEDICATION

To my parents, who love me and support me all the time.

ACKNOWLEDGEMENTS

I would like to express my full gratitude to my supervisor Professor Yvon Savaria and my co-supervisor Professor Mohamad Sawan, who all along this thesis were present to assist me. Providing me with the opportunity to work on this subject and good advice, they guided me towards more challenges in this research field.

I would like to thank CMC microsystems for providing access to technology and to design and simulation tools.

Profuse thanks go equally to Dr. François Leduc-Primeau and Dr. Yves Blaquiere for their participation to the jury of this thesis and their review of the text.

Special thanks to Mohamed Ali for his help in reviewing of the text.

RÉSUMÉ

Les capteurs sans fil sont intéressants dans de nombreuses applications telles que la surveillance de l'environnement, les soins de santé, la surveillance industrielle, le contrôle du trafic, l'agriculture et l'industrie alimentaire. Toutefois, la durée de vie d'un capteur sans fil est limitée par son alimentation électrique. Les piles sont généralement utilisées pour alimenter les capteurs sans fil. Elles souffrent cependant de diverses limitations, telles que les restrictions de taille, le coût associé au remplacement et l'énergie limitée fournie. Pour éviter ces limitations, des solutions sans piles pour les capteurs sans fil pourraient être considérées lorsque d'autres sources d'énergie permanentes sont nécessaires pour alimenter le capteur. Ces sources d'énergie comprennent l'énergie solaire collectée, les piles à combustible microbiennes et l'énergie collectée par RF. Cette dernière méthode est adoptée dans ce travail. Il convient de noter que les collecteurs d'énergie RF fournissent un budget de puissance très limité (de l'ordre du microwatt), de sorte que tous les éléments constitutifs des systèmes doivent être conçus pour consommer une puissance ultra-faible. Ce projet se concentre sur la conception d'une structure de capteur sans batterie avec récupération d'énergie par radiofréquence (RF) et une architecture est proposée pour cette application, implémentée avec MATLAB/Simulink pour en évaluer les performances. Cette architecture comporte cinq blocs principaux: un convertisseur AC-DC, une référence de courant, un oscillateur, un régulateur de tension et un circuit de réglage.

Une référence de courant à faible consommation d'énergie est conçue et simulée dans une technologie CMOS 0.18 µm dans l'environnement Cadence. Ensuite, cette source de courant est utilisée pour opérer un oscillateur en anneau à trois étages et fournit l'horloge du système. La fonctionnalité de l'oscillateur proposé a été validée par la simulation du circuit extrait du dessin des masques. De plus, une façon de changer l'oscillateur proposé en oscillateur contrôlé par tension (VCO) à ultra-faible consommation d'énergie avec le circuit de régulation est expliquée.

La boucle de calibrage de ce système est conçue. Elle se compose du détecteur de crête, du comparateur, du compteur et du bloc de conversion du code binaire en code thermomètre. Tous ces modules ont été conçus et simulés avec la technologie CMOS 0.18 µm.

ABSTRACT

Wireless sensors are attractive in many applications, such as environmental monitoring, healthcare, industrial monitoring, traffic control, agriculture, and the food industry. However, the lifetime of a wireless sensor is limited by its power supply.

Batteries are commonly used to power wireless sensors. However, they suffer from various limitations, such as size restrictions, costs associated with replacement, and the limited energy provided by the batteries. To avoid these limitations, battery-less solutions for wireless sensors could be considered in which other permanent sources of energy are required to supply the sensor. These energy sources include harvested solar energy, microbial fuel cells, and RF energy harvesting. The latter is considered in this work.

It is worth noting that RF energy harvesters provide a very limited power budget (in the microwatt range), so all systems' building blocks must be designed to consume ultra-low power. This project focuses on designing a battery-less sensor structure with radio frequency (RF) energy harvesting. One architecture is proposed for this purpose and it is implemented with MATLAB/Simulink to evaluate its performance. The architecture is composed of five main blocks: an AC-DC converter, a current reference, an oscillator, a shunt regulator, and a tuning circuit.

An ultra-low power current reference is designed and investigated. This work was performed using the parameters of a 0.18 μm CMOS technology in the Cadence environment. Afterwards, this current is forced to a three-stage ring oscillator, which provides the clock for the system; a very low power oscillator is designed, and the proper functionality of the proposed oscillator has been validated through post-layout simulation results. Furthermore, one way to adapt the proposed oscillator to obtain an ultra-low power regulated voltage-controlled oscillator (VCO) is explained.

The tuning loop for this system is proposed. It consists of a peak detector, a comparator, a counter and a binary to thermometer code conversion block, all of which have been designed and simulated with a 0.18 μm CMOS technology

TABLE OF CONTENTS

LIST OF TABLES

LIST OF FIGURES

LIST OF SYMBOLS AND ABBREVIATIONS

MOS	Metal oxide semiconductor
IoT	Internet of Thing
RF	Radio Frequency
ADC	Analog to Digital Converter
SAR	Successive Approximation Register
PoE	Power over Ethernet
PLC	Power-Line Communication
HWPLC	Hybrid Wireless and PLC
WSN	Wireless Sensor Network
FET	Field-Effect Transistor
NMOS	N-channel MOSFET
PMOS	P-channel MOSFET
CMOS	Complementary Metal-Oxide-Semiconductor
RFID	Radio Frequency Identification
WIFI	Wireless Fidelity
CMT	Cable Mode Transition
EDLC	Electrical Double Layer Capacitor
VCO	Voltage-Controlled Oscillator
PTAT	Proportional to Absolute Temperature
CTAT	Complementary to Absolute Temperature
FM	Frequency Modulation
MEMS	Micro electromechanical systems

MATLAB Matrix Laboratory, a numerical computing software

CHAPTER 1 INTRODUCTION

1.1 Definition of a Sensor

A sensor is a device that detects changes in physical quantities such as pressure, humidity, motion, heat, and light and returns an electrical output. For instance, a thermocouple converts changes in temperature into a variable voltage signal. The sensitivity of the sensor shows how much the output signal changes when the input quantity is varied. While the resolution of a sensor is defined as the smallest detectable change in the measured quantity. There are different kinds of sensors including electric thermostats, invented by Warren Johnson in 1883 and Infrared sensors which arrived in the market around the 1940s.

Also, a Metal Oxide Semiconductor (MOS) sensor was proposed in the 1930s, before bipolar transistors, but practical technologies to fabricate MOS appeared only in the early 1960s[1] . MOS devices can offer significant advantages including lower power consumption, low cost, the ability to work with lower supply voltages compared to bipolar transistors. In addition, MOS sensors have compact structures and can be designed to have very high-input impedance, which makes them very attractive for many sensor applications [1]. Many sensors based on MOS devices have been presented in the literature. Authors in [2] describe different types of Field Effect Transistors (FETs) based sensors. In the following sections, we will introduce the main types of sensors, including wired and wireless sensors.

1.2 Wired Sensors

Sensors with wires have been used for many years, therefore many engineering standards already exist for them and there is a good chance of finding wired sensors for a wide range of specific application. They are popular, inexpensive, exhibit low-power consumption and are often smaller than wireless sensors, because they do not need transceivers for communications. However, wired sensors may be less flexible due to required wiring. For example, in airplanes, many sensors are needed. All sensors associated with critical function must be doubled or tripled when it is possible. The cabling required for wired sensors contributes significantly to the weight of aircrafts that designers thrive to minimize.

There are many types of sensors such as Piezo-resistive thin gauge sensors [3] which are very popular because of their low cost. Optical fiber sensors are also attractive, since they are lightweight and can offer distributed sensing at discrete locations [4], however they offer suffer from high installation costs.

Some techniques for decreasing the number of wires have been presented including power over ethernet (PoE), power-line communications (PLC), and a combination of PoE, PLC and wireless system.

1.2.1 Power Over Ethernet

A Power over Ethernet (PoE) connection provides both power and data over a single cable. Transferring power over an ethernet has some advantages such as time and cost savings and flexibility, because it is possible to reduce the wiring. Also, some WIFI and Bluetooth RFID readers are POE-compatible devices, which allows access from remote locations away from AC power outlets.

The cost of installing and wiring sensors in large system can be very significant [5]. This cost can be reduced by using PoE.

Power consumption of systems comprising many sensors can be reduced by activating them when needed. A complete sensor system exploiting PoE is proposed in [6] and its hardware is composed of four parts: a switch, a power converter, a controller and a sensor unit. Another sensor network based on PoE is presented in [7].

1.2.2 Power-Line Communication (PLC)

Power-Line Communication (PLC) is a communication method in which data can be sent over existing power cables. In other words, with PLC, extra cabling is not needed; it re-uses existing wires. In terms of frequency, PLC networks can be partitioned in two categories: narrowband PLC and broadband PLC. The former is typically used for long distance communications, and it operates at low frequencies. By contrast, broadband PLC typically works at high frequencies and is used for short distance communications.

The PLC technique is a good choice for the so called internet of things (IoT) applications[8] because of its advantages, such as simplicity and low-cost [9]. However, it has some disadvantages, such as a reliability issue, due to the channel being changed by changing the load, topologies of the network, and location of the transmitter [10]. To solve the reliability issue, a relaying power line communication (PLC) network is proposed in [11]. The performance of the relaying PLC network is analyzed and investigated in [12]. In [13], both the channel and power of the sensor are optimized with the relaying PLC technique. Moreover, two ways relaying PLC, in which the information is exchanged between two sources, is proposed in [9].

1.2.3 Hybrid Topology

In certain applications, such as smart home networks, an Hybrid combination of Wireless and PLC (HWPLC) is a good solution [14]. Indeed, with PLC alone wireless devices, such as mobile users, cannot connect to the system [15]. As a result of its high efficiency, various hardware and software products have been developed to use HWPLC in an IoT network [16] [17],[18]. However, HWPLC systems suffer from a signal loss issue when used for long distance transmissions [19]. Several researchers focused on this problem and offered some solutions. One of these solutions based on relaying the PLC network was shown to be efficient as discussed in [13]. However, another problem with HWPLC is the very different characteristics of the wireless and PLC networks [20]. Some researchers have worked on mitigating this issue [21]. In [14], an HWPLC relaying sensor system is proposed and analyzed.

1.3 Wireless Sensor Network (WSN)

Typically, in an IoT domain, hundreds or thousands of sensor nodes could be used for monitoring purposes[22]. In such applications, wired sensors would increases the system deployment and maintenance costs. Such costs would be significantly reduced if the system is implemented with wireless nodes. On the other hand, wireless solutions may increase power consumption of individual sensors as communication mechanisms need extra power. This is one of the main challenges associated with wireless IoT nodes.

A Wireless Sensor Network (WSN) typically comprise a group of sensors that are used for monitoring environmental factors, such as humidity, pressure, motion, vibration or temperature.

The data collected by a WSN is typically sent to a main location for analysis. Each node of the WSN has a sensing unit, a transceiver for sending the measured information, and a power management module. Also, some nodes of a WSN may be equipped with an actuator to act upon certain conditions. In [23], wireless sensor and actuator networks are analyzed.

Since wireless nodes are battery-less or battery powered devices, reducing their power consumption is very important to allow energy efficient networks, which increases their lifetime. In [24], a Cable Mode Transition (CMT) algorithm is proposed, which determines the minimal number of active sensors in its network. While in [25], an algorithm for minimizing the delay in the data collection process for extending the lifetime of the network was proposed.

1.4 Applications of Wireless Sensors

Wireless sensors are attractive in many applications such as healthcare, industrial monitoring, traffic control, agriculture, and food industry [26],[27],[28].

They have many applications such as:

- Area monitoring [29]

Wireless sensors can be distributed in different places within one region to sense environmental changes such as temperature, pressure, humidity, and so on. In addition, they send back their information to the base stations for appropriate actions.

- Transportation[30],[31],[32]

Wireless sensors can monitor traffic information and can build a complete model of traffic. They provide an opportunity to solve issues surrounding traffic by providing traffic times to drivers as well as changing the timing of red lights, and to attempt to synchronize all traffic lights.

- Biomedical applications [33],[34]

Sensors are very common in the biomedical domain, where they are used to monitor patient's vital signs. This helps doctors monitoring and analysing patients' health condition over a long period of time. Doctors can also choose to use wireless sensors to monitor children who move a lot and cannot lay in a bed for a long time, since wired sensors would not be a good choice in monitoring children' health condition.

- Motion detection [35]

A motion detector uses one or multiple technologies to detect movement in certain area. It is very often used in many purposes, such as hand dryers, automatic doors, and at airports for counting the number of luggage loaded into an airplane.

- Food monitoring[36]

Food monitoring programs contribute to hazard identification and provide data to inform the quantification of exposure. Also, when delivering food over a long period of time, monitoring is important to see whether it remains fresh and safe to consume. For example, in meat inspection, which is described in [37].

- Air pollution monitoring[38],[39]

Nowadays, air pollution is a major problem in all countries. Air pollution damages animals, forests, and humans. It also contributes to the depletion of the ozone layer, which protects the Earth from the UV rays of the sun. Moreover, acid rain is another major problem caused by air pollution. Another environmental effect of air pollution includes global climate change, which is one of the most important concerns for all people. With the help of these sensors, we can monitor air pollution periodically and take action when necessary.

- Forest fire detection[40]

Wildfires are unwanted and uncontrolled fires in a large area, which can be very dangerous. Controlling wildfires is very difficult, so it is a good idea to identify a fire quickly after it starts, and then try to control it as early as possible.

1.5 Wireless Sensor Network Topologies

In a WSN, sensor nodes are connected in different configurations, including star, mesh, and hybrid topologies [41]. These different topologies will be described in the following sections.

1.5.1 Star structure

As shown in Figure 1.1, with the star structure, only one base station is present and it receives the data from each node of the network, while theses nodes cannot communicate with each other. The main benefit of this structure is its simplicity.

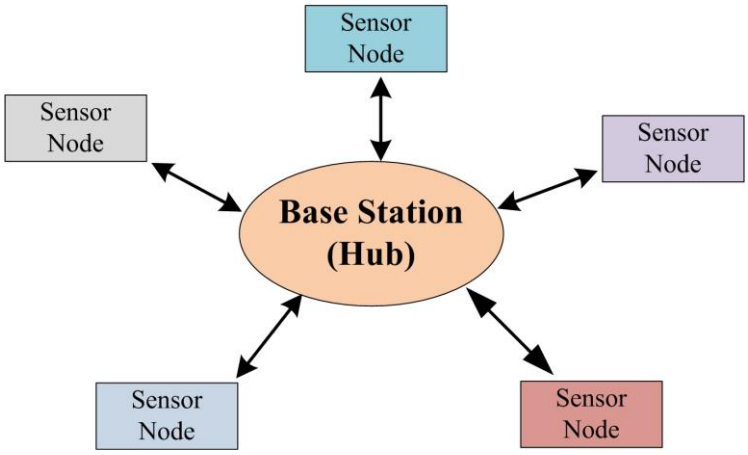

Figure 1.1 Star network topology.

1.5.2 Mesh structure

Figure 1.2 illustrates the mesh structure, where each sensor nodes can communicate with the other nodes. In addition to its complexity, mesh topology has higher power consumption, because each node needs more power.

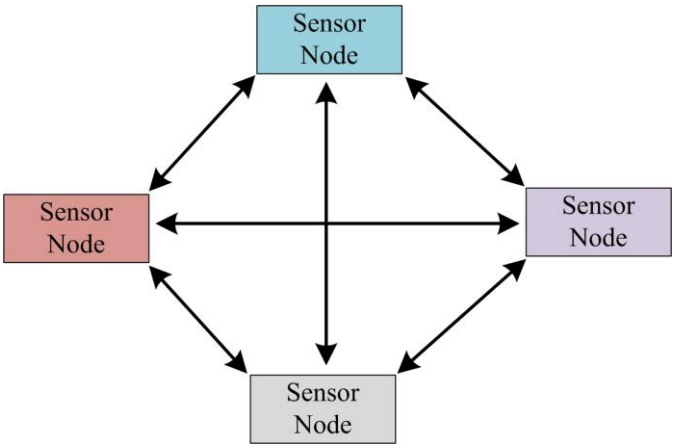

Figure 1.2 Mesh network topology.

1.5.3 Hybrid star – Mesh structure

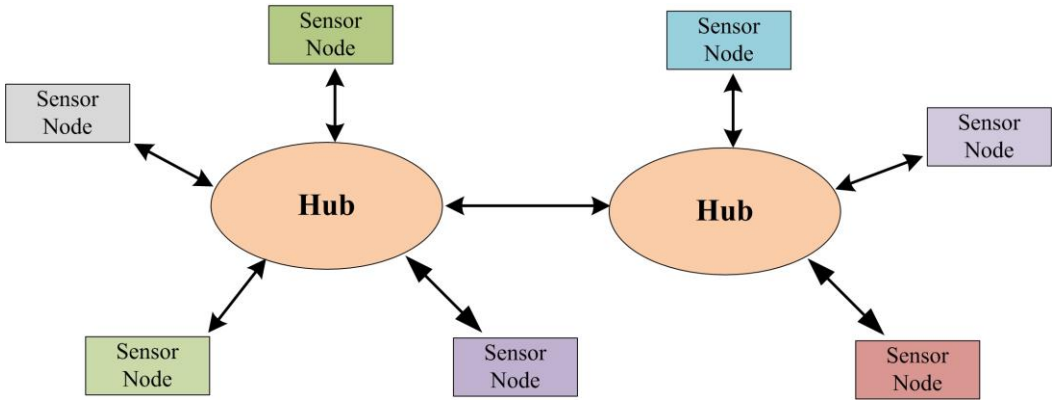

Figure 1.3 Hybrid network topology.

This structure provides a robust network and consumes less power than a mesh structure. As depicted in Figure 1.3, in this topology, each sensor node communicates with only one other node, which decreases the system's power consumption.

1.6 Wireless Battery-less Sensor Node

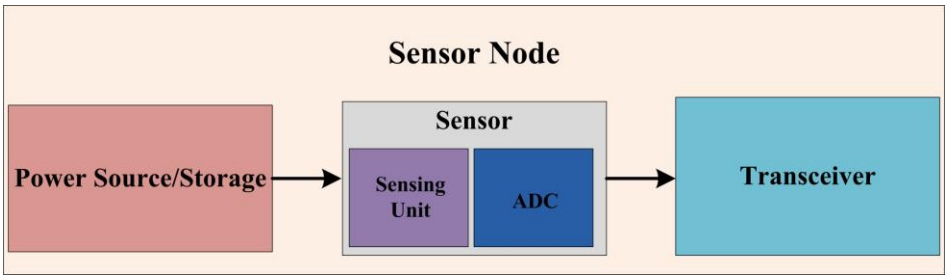

Figure 1.4 Internal structure of a wireless sensor node.

Various monitoring applications, such as environment, necessitate sensor nodes to cover a large land area. Wireless sensors are suitable for this kind of applications, since wireless communications provide extra flexibility for the system.

As shown in Figure 1.4, a sensor node consists of three main parts: a sensor, a transceiver, and a power unit. The sensor unit involves a sensing unit and an analog-to-digital converter (ADC) [42]. The sensed data is converted into digital code and sent to the base station for further processing. The power source/storage unit is one of the most important parts of the sensor nodes, which may or may not comprise a battery when energy comes from a harvester.

Sensor nodes are usually battery-operated devices [43] and hence, their lifetime are limited by the energy/power budget of the battery. In addition, batteries suffer from various limitations, such as their size and costs associated with replacement, especially if the sensor nodes are integrated in harsh environment, and limited energy is provided. Various techniques were presented to reduce the power consumption of sensor nodes such as energy-efficient routing protocols [44]. Applying these techniques extends the lifetime of the node's battery. Also, self-discharging problem associated with batteries decrease the batteries' lifetime.

To avoid these limitations, battery-less solutions for wireless sensors could be considered, where other permanent sources of energy are required to supply the sensor node. For this reason, different kinds of devices have been developed to provide and store energy. For instance electric power can be generated from temperature by thermoelectric devices or from sunlight by solar cells [3].

Moreover, electrical energy can also by extracted from surface acoustic waves (SAW). These signals are collected by an antenna, processed and converted into a DC signal. However, SAW are low frequency signals and hence a large antenna should be employed to collect these signals. This results in bulky sensor nodes that also suffer from additional loss because of the double conversion between electrical and mechanical signals [47].

In addition to the aforementioned powering systems, microbial fuel cells, and RF energy harvesting [48],[49],[50] could be employed to allow battery-less wireless sensor node implementation. However, these sources usually provide very limited energy budget; this also depends on the source of the energy and the physical size of the devices that are used to provide these types of energy. One solution is the use of the electric double layer capacitor (EDLC) technique, which allows the sensor to store energy and to use it for limited operation. It is also common that energy storage devices are charged over a long time while the sensor node can operate only for a short time.

For some applications, a short delay in communications is acceptable; for example, when sensing the temperature or pressure and the loss of some sensed data elements can be recovered through mathematical methods that interpolate missing data. However, delays in communication may not be acceptable in applications where urgent events are sensed and must be transferred quickly.

The power ratings from mW to W for the implantable wireless sensors have been discussed in [51],[52]. Transmitting data and power delivery with only one pair of the inductance coils is investigated in [53] and the system can deliver up to 94 mW and eight switch-capacitors are used for extending the wireless power regulation range. Meanwhile, sensors with less power consumption (tens-μW) are essential for many therapeutics that are yet to come [54]. An example of Wireless power transfer system that offers ultra-low power consumption was reported in [55].

PLL-based implantable biosensor which is wirelessly powered by RF energy harvesting is reported in [56]. It consumes only 4 μW and backscattering technique is used for sending back the data. A microsystem which is powered wirelessly and transmitting data with backscattering technique is described in [57], it consumes 225 μW and this power is delivered with the external transmitter and the main contribution of this work is providing a 64-channel recording platform with the area and power reduction technique.

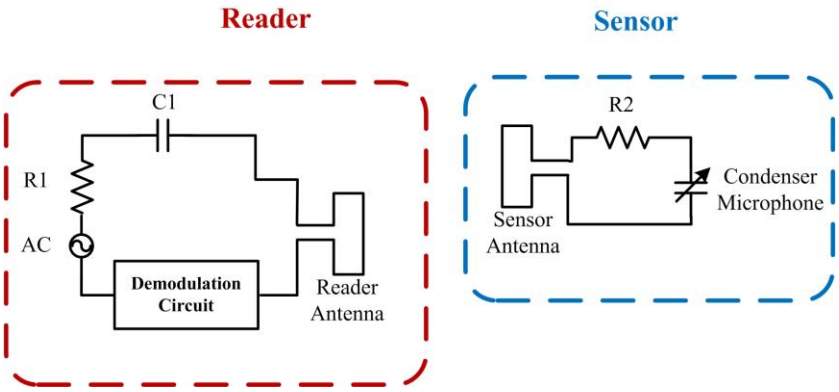

Figure 1.5 Reader and sensor units of a wireless sensor node.

CMOS multi-sensor SoC was presented in [58] and since it dissipates a power of 942.9 µW, two sources of the energy (RF and light) are used for delivering power and it is a good candidate for monitoring the temperature and the protein concentration in biomedical applications and the main feature of this work is the capability of generating the four types (C, R, I, V) sensing signal which can show the physiological parameters simultaneously.

Another implantable microstimulator system on chip (IMSoC) work was demonstrated in [59] and it consumes 48 µW and two off-chip rechargeable batteries are used for providing the power of the system. The 10-bit implantable blood pressure sensor is described in [60]. The total power consumption of the system is 300 µW and is provided by RF energy harvesting and also the sensed data is transmitted wirelessly in a frequency of 433 MHz and it is suitable for small animals because of its low weight and it has a good sensing resolution which is 1mmHg over 1 kHz with a signal to noise distortion ratio (SNDR) of 60 dB.

Authors in [61] describes a wireless battery-less sensor. According to Figure 1.5, it has two parts, a reader unit and a sensor unit. The sensor unit has a condenser microphone and an antenna coil. The capacitance of the condenser microphone and the inductance of the antenna create a resonance frequency. The capacitance of the microphone changes with the acoustic waves and as a result the resonance frequency changes. The reader unit produces the alternating current, which is delivered to the sensor unit through the electromagnetic field, so that the sensor unit draws energy from the reader side and causes the voltage to drop. By changing the impedance of the sensor unit, the

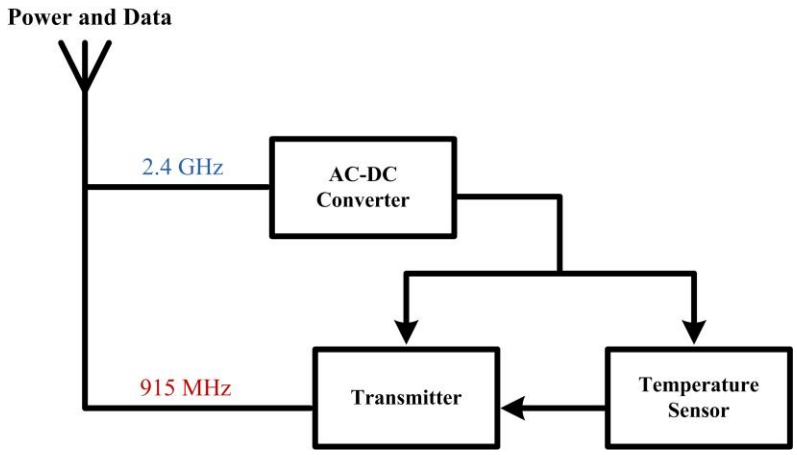

Figure 1.6 Collecting both power and transmitting data with the antenna.

voltage drop at the reader side changes. The condenser capacitance changes with the acoustic waves, and the reflected impedance of the sensor unit can determine the magnitude of the voltage drop in the reader's side. This technique is useful to capture voice and lung sounds. It is thus a good choice to monitor patients with pulmonary diseases. As such sensor can be small and wireless, it can easily be attached to the body.

An analog to digital converter (ADC) - based sensor is shown in [62],[63]. These authors claim that successive approximation register (SAR) ADCs are best suited to sensor nodes. Indeed, in these two papers, a very energy efficient ADC is used, and it shown that it can work with an energy harvester. A high resolution (i.e.12-bit) could be achieved to increase the sensitivity of the sensor. These sensors have two resolution modes, 12-bit at 100 kS/s and 8-bit at 200 kS/s. However, both modes consume 25 µW from 1 V, which is a little high for RF energy harvesting or even if the RF energy harvesting is used for them. The read range (i.e. the distance from the RF source that the sensor can work properly) would be very low with this level of energy consumption.

Authors in [64] presents a complete system for sensing the temperature in biomedical applications. According to Figure 1.6, it consists of a radio frequency (RF) to DC converter, a temperature sensor, and a transmitter. In this work, one antenna is used for collecting both power and for transmitting data. The 902 to 928 MHz frequency band was used to transmit data because the loss

at these frequencies is low in the body while the 2.4 GHz frequency was used for delivering power. In addition, a low-power FM transmitter is used to send the measured data back to the base station. This transmitter consists of a voltage-controlled oscillator (VCO) and one buffer to improve the capability of the transmitter. For sensing, a current sensitive to temperature and proportional to absolute temperature (PTAT) is generated. Moreover, the total power consumption of this system is 109.6 μW, which is high for RF energy harvesting.

In a complete pressure sensor system is presented in [65]. This system consists of a RF to DC converter (rectifier), a sensing unit, a voltage regulator, a voltage reference, and a transmitter. A 5.23 pF Micro electromechanical systems (MEMS) capacitor with 6.64 fF/mmHg sensitivity was used in the sensor unit. These parameters were deemed suitable for pressure sensors and to communicate data, a VCO was used to frequency modulate the data before sending them with transmitter.

1.7 Thesis Objectives, Contributions and Methodologies

This work aims to:

- Propose a wireless battery-less system to sense environment factors.
- Design its various building blocks as low power circuits.
- Validate the functionality of the proposed design using proper CAD tools.

In this thesis, a wireless battery-less sensor is proposed. It is meant to operate by harvesting energy from RF. The proposed wireless battery-less sensor consists of five main blocks: AC-DC converter, oscillator, shunt regulator, peak detector, and tuning circuit.

The main contribution of this thesis has been reported in a conference paper, published in 2020

IEEE International Conference on Electronics Circuits and Systems (ICECS) [66].

1.7.1 Methodology

To achieve the stated objectives, a suitable system architecture and effective circuit implementation of each block must be chosen to minimize the power consumption. This is necessary for the related sensor node to be compatible with RF energy harvesting. Based on a thorough literature review,

model is proposed and implemented with Simulink/MATLAB to evaluate the expected performance. The steps that were followed are listed below;

1) A suitable technique for sensing was proposed;

2) A detailed review of literature review on means to implement the various blocks was performed;

3) A complete system architecture was proposed;

4) Target specifications were defined;

5) The critical blocks of this system were implemented at transistor level and their performance was evaluated.

1.8 Thesis Outline

This thesis is organized as follows: The proposed battery-less sensor is explained and investigated in Chapter 2. In Chapter 3, the critical blocks of the proposed system are designed, and the simulation results validating them are reported. Finally, Chapter 4 summarizes the work reported in this thesis and some concluding remarks are given.

CHAPTER 2 BASIC CONCEPTS AND OVERVIEW OF THE PROPOSED SYSTEM

This chapter presents the architecture of the proposed battery-less wireless sensor exploiting an RF energy harvesting technique. Also, the functionality of the proposed system is validated at the system-level using MATLAB. Moreover, the feasibility of the various critical blocks is assessed in order to define their specifications.

2.1 Basic Concepts

A key module of the type of wireless electronic object that is proposed in the thesis is its antenna. As shown in Figure 2.1, an antenna can be modeled as the parallel combination of a resistor, a capacitor and an inductor [65].

The quality factor Q of a resonant parallel RLC circuit is defined as:

$$Q = \frac{\omega_0}{2\alpha} = \frac{R}{\sqrt{L/C}} \qquad 2.1$$

To reduce the energy loss in the circuit, we must decrease any series resistance. However, according to Equation 2.1, for less damping, the parallel equivalent resistance of the parallel RLC model should be increased to allow high Q factor.

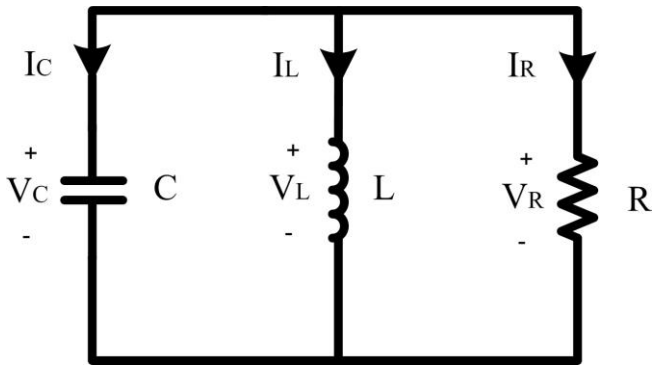

Figure 2.1 Parallel RLC circuit

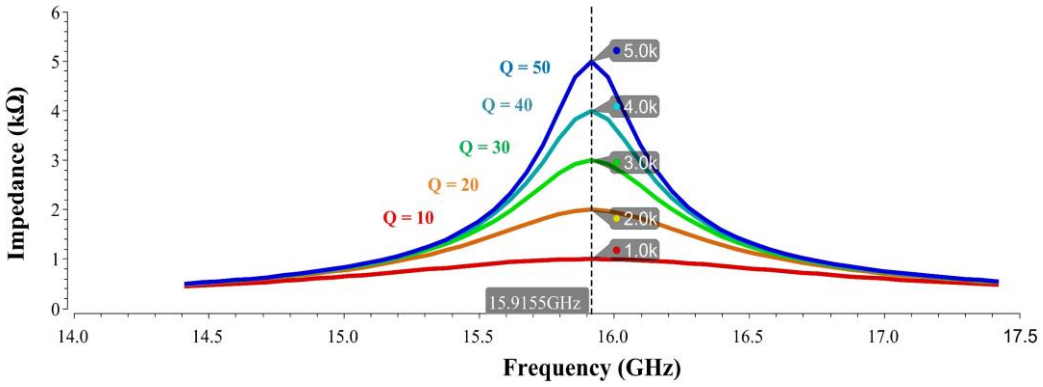

Figure 2.2 Q factor of the parallel RLC circuit.

Resonance occurs when the imaginary part of the admittance of the parallel RLC circuit becomes zero.

$$X_L = X_C \tag{2.2}$$

$$2\pi\, fr\, L = \frac{1}{j2\pi fr\, C} \tag{2.3}$$

$$fr = \frac{1}{2\pi\sqrt{LC}} \tag{2.4}$$

Where f_r is the resonance frequency.

To understand the relation between the quality factor and impedance, the impedance versus frequency for different resistance values and constant L = 1nH and C = 100fF are shown in Figure 2.2. In that case:

$$fr = \frac{1}{2\pi\sqrt{LC}} = \frac{1}{2\pi\sqrt{1n \times 100f}} \approx 15.91GHz \tag{2.5}$$

$$\text{For } R = 5k\Omega, \quad Q = \frac{\omega_0}{2\alpha} = \frac{R}{\sqrt{L/C}} = 50 \tag{2.6}$$

Other values are shown in table 2.1.

Table 2.1 Q Factor Values for Different Resistors

R (kΩ)	1	2	3	4	5
Q	10	20	30	40	50

In conclusion, the maximum power theorem says that the source and load impedances must be complex conjugates of each other.

2.1.1 Bandwidth of the Antenna

The bandwidth of an antenna is defined by the range of frequencies that the antenna can operate at, and out of that range of frequencies, a signal is not detected by the antenna which is shown in Figure 2.3. Some key relationship related to bandwidth are as follows:

$$BW = f_{upper} - f_{lower} = \frac{fr}{Q} \tag{2.7}$$

Where, f_{upper} and f_{lower} are the upper and lower cut-off frequencies, respectively. At f_{upper} and f_{lower}, the power that can be dissipated in the circuit is half of the full power dissipated at the resonant frequency, which is $0.5(I^2 R)$.

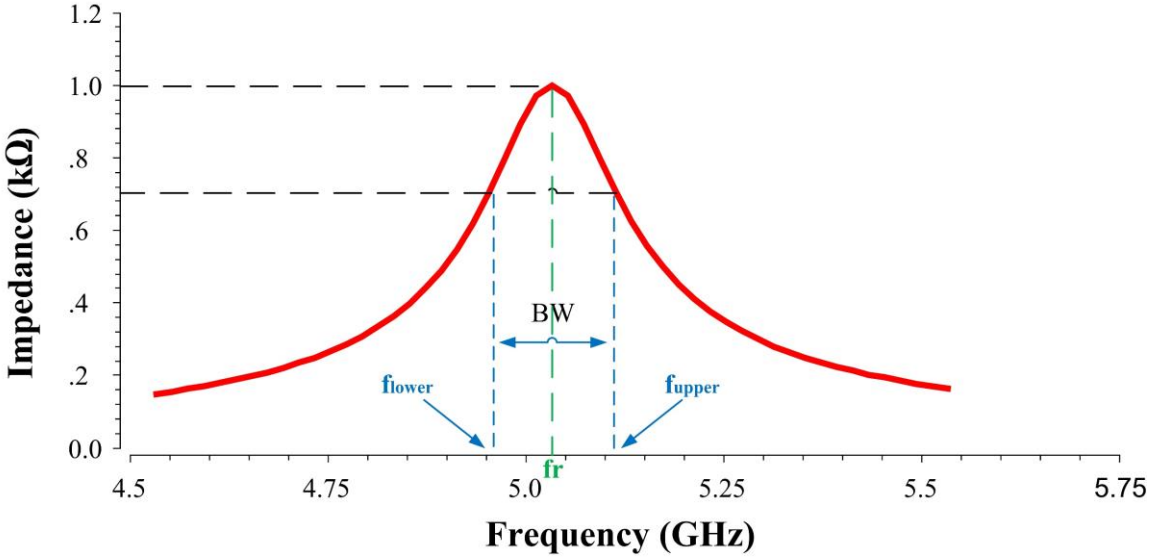

Figure 2.3 Bandwidth of an antenna

In a resonant system, if the ratio between inductance and capacitance in an RLC configuration changes, the resonance frequency changes, and consequently, the range of frequencies that pass through the antenna also changes (Equation 2.7). It is also of interest that for maximum power transfer, the transmitter frequency should be at the middle of the antenna's bandwidth. Therefore, it is important to adjust the bandwidth of the antenna by suitably tuning its resonance. For tuning, there are two possible solutions:

1. Passive tuning

With passive tuning, the respective reactance of the inductor and capacitor must be suitably selected.

2. Active tuning

It can be done by changing the reactance of the inductor and capacitor with variable component. For instance, this can be done with varactors. Figure 2.4 shows a system with active tuning in which a variable capacitor is used to set the resonance frequency of the circuit at the middle of the

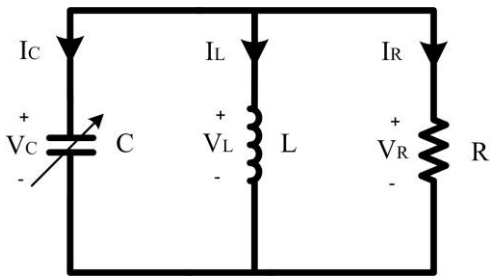

Figure 2.4 Tunable RLC circuit

passband of the antenna. Thus, in a system in which the transmitter frequency is fixed, any environmental factor changing the inductance can be sensed by tuning the circuit with a variable capacitor. For example, if the humidity changes in the environment, the inductance of the antenna will change. As a result, to reach the maximum power transfer condition, we must change the capacitance until we reach the maximum output power. The value of the capacitor in the new condition reflects the variation in the environment, such as the ambient humidity.

2.2 System Architecture of a Proposed Battery-less Wireless Sensor Chip

If we want to use RF energy harvesting to eliminate or to reduced reliance on a battery, an architecture with very low power consumption blocks is required because the budget for power is very limited. First, an AC to DC converter is required to convert the RF signal to the DC voltage that provides the DC supply voltage for the other blocks.

A circuit is needed to detect when maximum power delivery is reached. Another module is needed to adjust the value of the tuning capacitor in the front end. The proposed block diagram also comprises a module that provides a clock for the entire system and one block that protects the system when the instantaneous received power is too high.

Figure 2.5 shows the architecture of the proposed battery-less sensor chip and its associated antenna used to collect RF signals and as a sensing element.

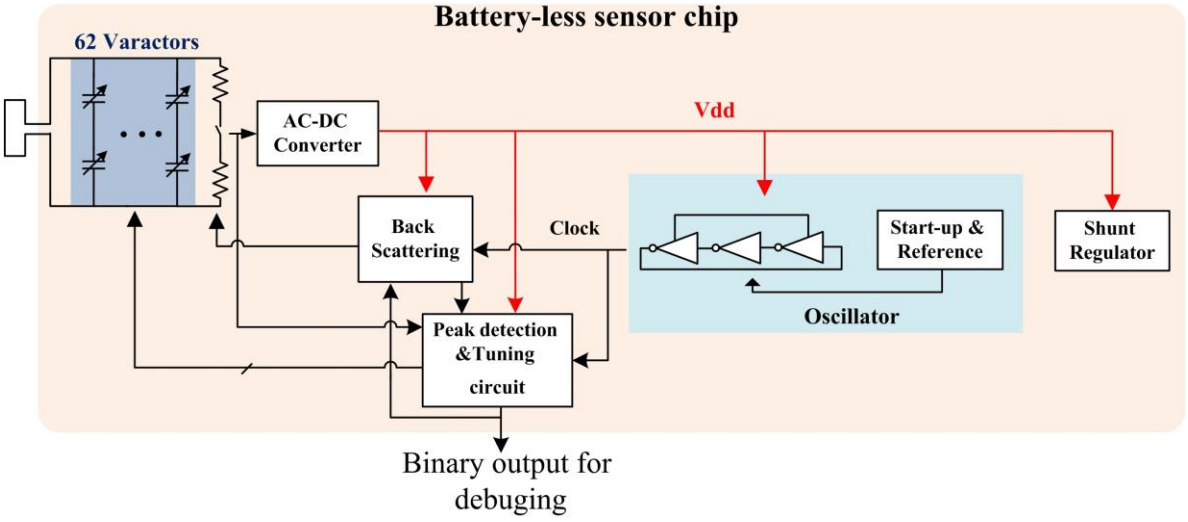

Figure 2.5 Block diagram of the proposed battery-less sensor chip.

The AC-DC converter receives the RF signals from the antenna and provides a DC output voltage. This voltage is then regulated with a shunt regulator that supplies power to the various circuits of the sensor. In addition, a matching network composed of an array of 62 varactors needed to obtain a 5-bit resolution (each thermometer output controls two varactors) is utilized before the AC-DC converter to set the circuit at its resonance frequency to achieve maximum power delivery. In order for the signal to noise ratio (SNR) to remain manageable, 5-bit resolution is considered for this system. Therefore, when the antenna inductance changes because of a change in the environment, such as humidity, the generated voltage from the AC-DC converter varies. Thus, a tuning loop is proposed to achieve maximum power delivery. This loop exploits a peak detector, a counter, and a block to convert the binary code provided by the counter to a thermometer code. A peak detector circuit is used to monitor the voltage generated by the AC-DC converter and to set the value of an up/down counter accordingly. This information can be used to tune the matching network until the voltage provided from the AC-DC converter reaches its peak. The binary code generated by the counter reflects the state of the environment when the loop settles.

In the proposed architecture, an array of 62 varactors is used to tune the matching network. The capacitance of these varactors is changed via an applied biasing voltage. Adjusting capacitance

with varactors is preferred to the use of switched capacitors to obtain a lower series resistance compared to a combination of switches and capacitors. The binary code, which is generated by the tuning circuit, is converted to a thermometer code controlling the varactors. An oscillator is employed to provide a clock to the counter circuit, which is used in the tuning block. Since the power budget in the proposed battery-less sensor is very limited, an ultra-low power oscillator design is required. Moreover, the power consumption of the oscillator circuit should be independent of temperature variations, as the sensor may need to operate over a wide range of ambient temperatures with the same power consumption, thus a reference (bias) circuit is needed to stabilize its operation.

The back scattering technique is adopted as a means to transmit the measured data for more analysis. In this block, a counter starts counting until a specific value is reached. This determines the sensing time sampling intervals. After this time, it sends a freezing command to the counter in the tuning loop and the binary code, generated by the tuning loop, must be sent back. For this purpose, two resistors and one MOS switch are used. To transmit 0, the switch is open, and the transceiver sees minimum reflection from the antenna, and to transmit 1, the switch is closed, and more reflection is detected by the transceiver. The signal which is detected by the transceiver is shown in Figure 2.6.

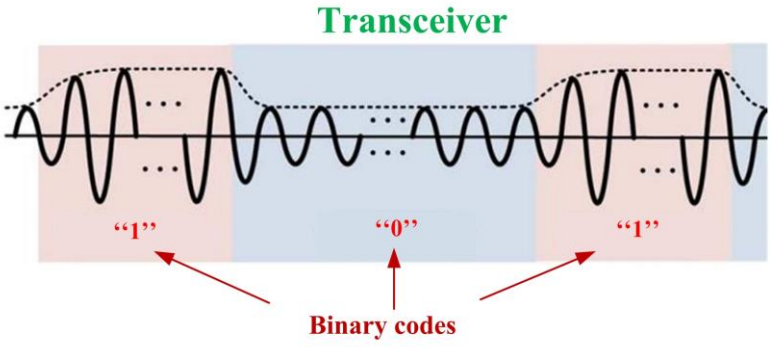

Figure 2.6 Typical signal observed with the back scattering technique.

As a result, the transceiver sees the large difference in the signal reflected by the antenna. Therefore, with this technique, we can code the measurement value and the transceiver can detect this code. To debug the system, one pin in IC is designed to measure the sensing value of this sensor chip.

2.3 System Level Implementation

As a first step towards implementing our proposed battery-less sensor, the behavioural model of the system, shown in Figure 2.7, was built using MATLAB®. The AC-DC converter is modelled linearly with an approximate model [50]. According to that model, the efficiency is 42.8%. The extracted power from the antenna depends on the distance between the antenna and the RF source. If the antenna is close to the RF source, it can provide more power compared to when there is a greater distance from the RF source.

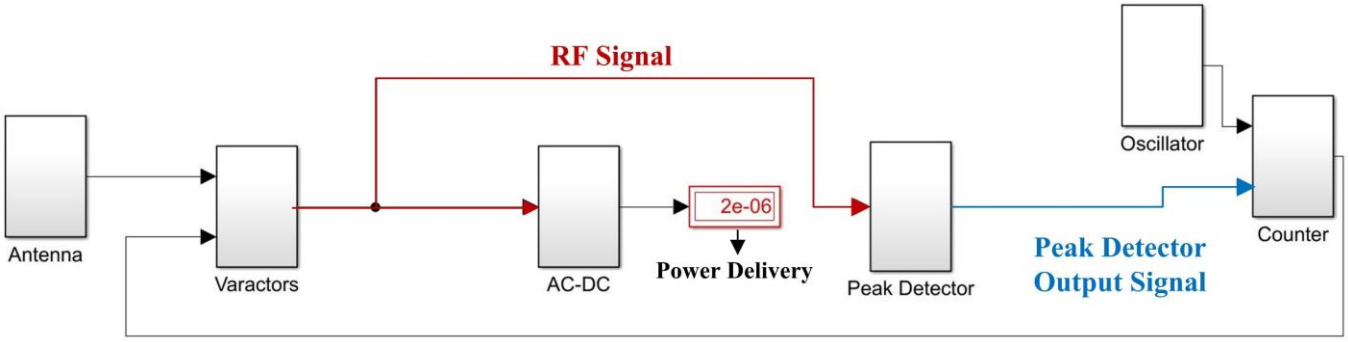

Figure 2.7 System modeling in MATLAB.

The power extracted from the antenna is multiplied by α, where α is set by the matching impedance between the inductance of the antenna and capacitance of the varactors and in this model, α is considered as a constant number. In the peak detector block, the peak of the signal is detected and compared with the previous peak value and the upward or downward signal is sent to the counter. Accordingly, the counter changes the parameter α in the varactor block each time until setting the circuit at its resonance frequency.

Figure 2.8 shows the transient simulation results of the proposed system and also reveals how the power delivered is changed as a function of the value of α that is considered as a constant in this

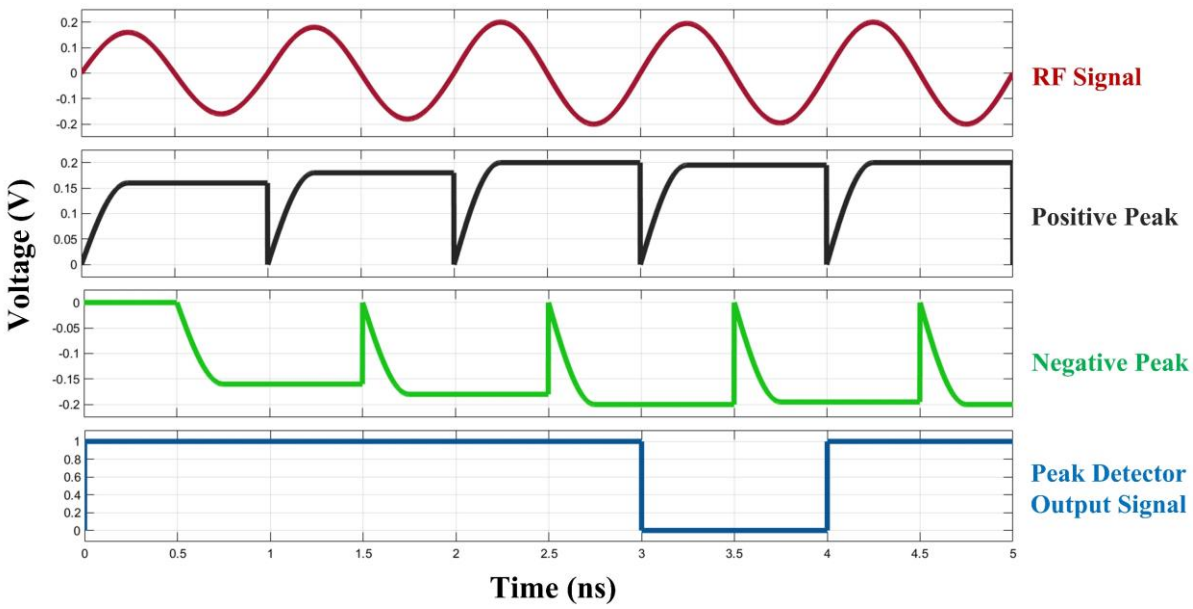

Figure 2.8 Simulation of the behavioral model of the proposed design.

behavioural model. The results are summarized in Table 2.2. Initially, the system receives 1.6 µW and after changing the varactors by one step (increasing the value of two more varactors), the received power improved to 1.8 µW. Consequently, the peak detector sends an upward signal, and the varactor increases by another step. The power then reaches 2 µW which is the maximum power, and again, the peak detector sends the upward command to the counter and the power decreases to 1.9 µW. Since the power is reduced, the peak detector sends the downward command at this time and the power again comes back to its peak value. Then the system begins oscillating between these two values. At that time, we consider that the optimal setting is settled as the system oscillates around its optimal point that can rapidly track any changing external condition.

Table 2.2 Behavioral Model for Power Transient

Parameter	T1	T2	T3	T4	T5
Power (µW)	1.6	1.8	2	1.9	2
Peak detector	1	1	1	0	1
Counter	10011	10100	10101	10110	10101

2.4 Subthreshold region

Since RF harvesting is used in our proposed system to provide power, all building blocks must be designed with ultra-low power consumption, so that they can work with the limited harvested power by the RF harvester, which is around several microwatts. Therefore, it is very important to know which region of the operation of the MOS transistor is suitable for designing such circuits.

When the gate-source voltage is lower than transistor's threshold voltage, the minority carriers are present under the gate. This is called subthreshold, or weak inversion region. Simulation results of both absolute and logarithmic plots of drain current of an NMOS transistor versus its gate-source voltage implemented in 180 nm technology are shown in Figure 2.9 and Figure 2.10, respectively.

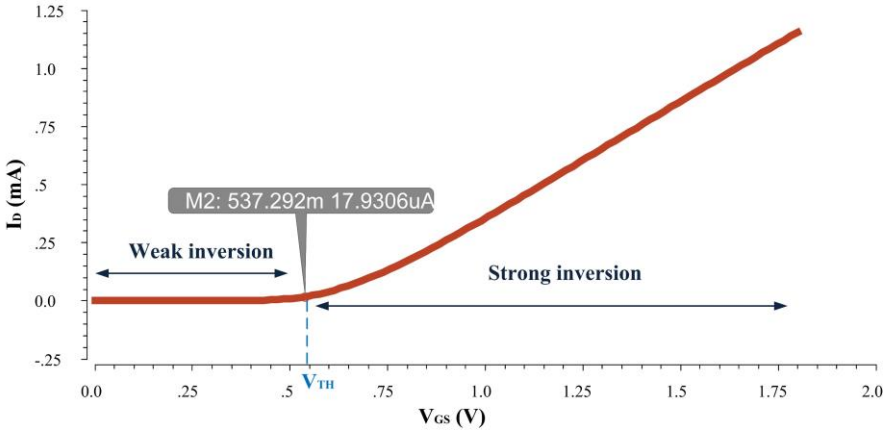

Figure 2.9 Drain current of the NMOS transistor versus gate-source voltage

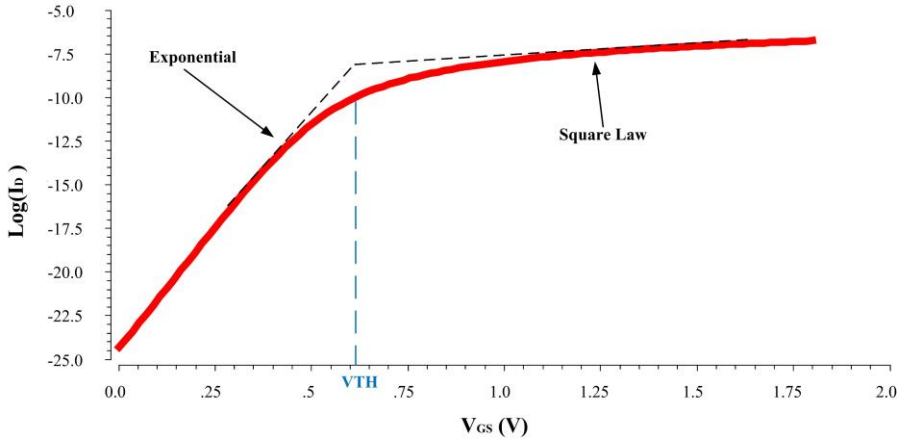

Figure 2.10 Logarithm of the drain current versus gate-source voltage of an NMOS transistor

At first, especially in the digital domain, the weak inversion region is viewed as a problem (i.e. leakage current), but nowadays, this mode of operation in MOS transistors has a lot of applications and it is as important as the strong inversion.

In a weak inversion, like the strong inversion, we have two regions of the operation. Because it is in saturation, the V_{DS} must be approximately larger than 100mV, and the current formula in this region can be written as,

$$I_D = I_0 \exp \frac{V_{GS}}{\xi V_T} \qquad 2.26$$

Where $\xi > 1$ is a nonideality factor, I_0 is proportional to W/L and V_T is a thermal voltage and is equal to kT/q, k is a Boltzmann constant, and q is the electrical charge on the electrons [1].

Since this equation is similar to that of the bipolar transistor, and with typical values of ξ, at room temperature, V_{GS} must decrease by approximately 80 mV to decrease I_D by one decade [1].

For a quick comparison between the strong and weak inversions:

a. Strong inversion

- Two regions of the operation (saturation and triode)
- Need $V_{DS} > (V_{GS} - V_{TH}) = V_{OV}$ to be in saturation
- Fast speed because of the high current

- Poor gm efficiency (i.e., $\frac{g_m}{I_D}$ is low)
- $gm = \frac{2I_D}{(V_{GS} - V_{TH})}$

b. Weak inversion

- Two regions of the operation
- Need $V_{DS} > 100mV$ to be in saturation
- Slow speed because of the low current
- Good gm efficiency (i.e., $\frac{g_m}{I_D}$ is high)
- $gm = \frac{I_D}{\xi V_T}$

According to the information presented above, the weak inversion (subthreshold) region is the best choice for this application, in which low power is essential.

2.5 Feasibility

We believe that RF energy harvesting is a strong candidate for wireless battery-less sensor because it is not time dependent; for instance, the energy, which comes from solar or wind, varies over time due to weather conditions. The other benefits of using RF energy harvesting include the availability of this source of energy, which is available everywhere, especially where other energy sources, such as vibration or thermal, are limited [68].

Since the power of the RF energy harvesting is very limited and it is around several microwatts [69], the feasibility check for some of the blocks in the proposed system is very important and essential before starting on the design of the subsystems.

2.5.1 AC-DC converter

An AC-DC converter unit, which is shown in Figure 2.11, is used to provide the supply voltage for the system's building blocks. There are different techniques for designing the AC- DC converter for RF energy harvesting, which are presented in the literature.

A voltage doubler-based AC-DC converter was presented in [69]. However, this technique shows limited efficiency (9.1 % at 900MHz and 8.9 % at 2GHz). Controlling the threshold voltage dynamically through the main transistors with the auxiliary transistor is another technique that is

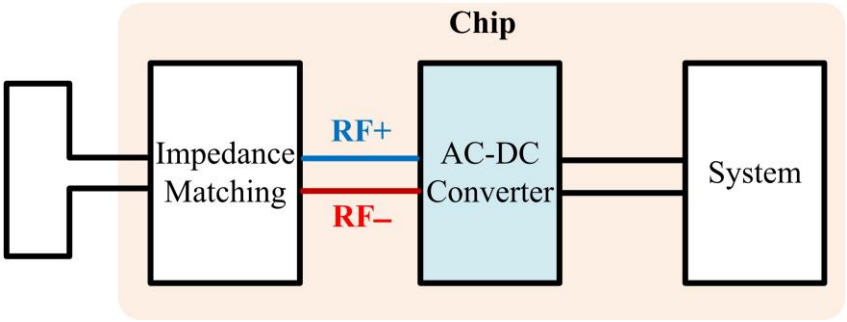

Figure 2.11 Sensor architecture

used in [70]. This technique is based on reducing the threshold voltage in forward biasing to increase the harvested power and to increase the threshold voltage at the reversed bias to reduce the leakage current and to reduce the loss of previously stored energy. As a result, a 12-stage adaptive threshold-compensated rectifier was presented for this method [47]. This technique showed an efficiency of 32 % at -15 dBm input, but for lower input, this efficiency is limited to 11%.

Cross coupled topology is another architecture that is widely used because of its good features such as low voltage, self-starting circuit and dynamic threshold voltage compensation [36].

In [71], a bootstrapped capacitor is used to reduce the effective threshold voltage. With this technique, the power efficiency at low frequency is increased (37 % at 0.8V in the source input). However, it shows bad performance when operates with high-frequency input. Thus, this technique is not efficient for RF energy harvesting.

In [50], dynamic and static bias compensation were used to decrease the transistors forward voltage drop. This method showed an efficiency of 42.8% at -16 dBm input power and a frequency of 915 MHz. This AC to DC converter generated an output DC voltage of 2.32 V on a 0.5 MΩ load. Due to its good efficiency obtained, this technique is adopted in our proposed design.

2.5.2 Current reference

A current reference generator is needed in the proposed sensor to provide the constant current for the other blocks. The generated current should be independent to supply voltage and temperature

variations, to minimize the impact on the consumed power by the various blocks in the system such as the oscillator.

Different techniques of robust current reference generators were reported in literature. In [72], two PTAT (proportional to absolute temperature) currents are subtracted from each other to produce a constant current with the temperature variation.

In addition, this design showed ultra-lower power consumption (45.8 nW). All of the transistors are in the weak inversion region, which is suitable for this application, and its current variation with temperature is about 186 ppm/^{o}C.

In [73], one complementary to absolute temperature (CTAT) and one PTAT current are added together to provide a constant current versus temperature. This design consumes 24 µW and shows 57 ppm/^{o}C current variation with temperature.

2.5.3 Oscillator

The oscillator circuit is a key circuit in the proposed sensor. It is used to generate the clock signal that drive the counter. Two main oscillator designs can be taken into consideration: an LC-oscillator and a ring oscillator. Although LC-oscillators provide linear and stable performance, especially at low frequency, they have some limitations, such as high-power consumption compared to ring oscillators. In addition, LC-oscillators occupy a large area of silicon as a result of the employed inductors and capacitors. On the other hand, ring oscillators achieve lower-power consumption and smaller silicon area. Various low-frequency and low-power oscillators were presented in the literature. In[74], a ring oscillator is introduced, which consumes 470 nW with a frequency variation of ±60 ppm/^{o}C. Another ring oscillator is presented in [75], where its power consumption is 280 nW with the frequency variation of ±52.5 ppm/^{o}C. An ultra-low power consumption (72nW) oscillator was presented in [76] with the temperature dependency of 148 ppm/^{o}C.

In this chapter, the proposed battery-less sensor node was presented, and its model was implemented with Simulink/MATLAB to evaluate the expected performance. Besides, a feasibility study was done to understand the power budget for the total system and for each building block.

CHAPTER 3 PROPOSED CIRCUIT LEVEL IMPLEMENTATION

This chapter presents the circuit level implementation of the critical blocks of the proposed system and it consists of four main sections: current reference, oscillator, tuning block, and shunt regulator. In addition, the tuning block part is composed of a peak detector, an array of varactors, and binary to thermometer code conversion circuit, which are investigated in this section. In the following sections, we provide a detailed explanation for each circuit and the critical circuits have been implemented and simulated using a 0.18 µm CMOS technology in the Cadence environment.

3.1 Current Reference Generator

Voltage and current references are very important in analog circuits to allow stable operation with temperature and supply voltage variations. A current reference circuits provide a DC current that

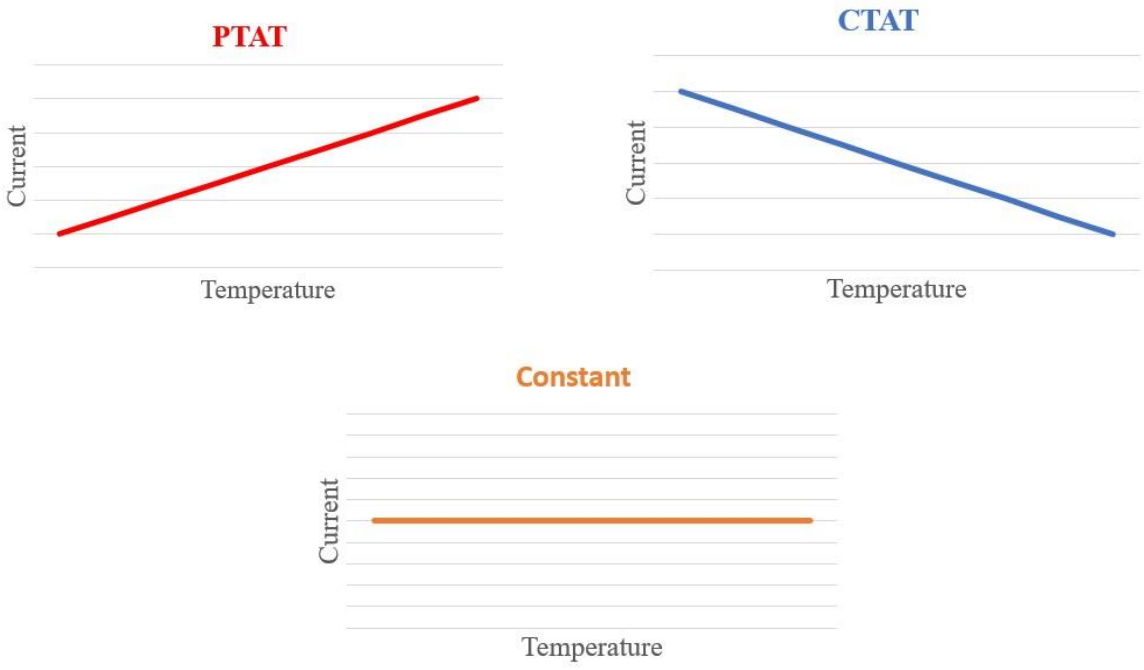

Figure 3.1 Different forms of dependency to the temperature

has little dependency on temperature and supply variations. Thus, two important parameters for reference circuits are considered:

- Supply independent biasing
- Temperature variations

In most applications, we can observe three forms of dependency to temperature as shown in Figure 3.1. The dependency can be:

1. Proportional to absolute temperature (PTAT);
2. Complementary to absolute temperature (CTAT);
3. Temperature independent.

Various techniques were proposed in the literature to obtain circuits independent to temperature, such as subtracting two PTAT currents from each other [48] and adding one PTAT and one CTAT current [49]. A common strategy is to provide two equations that vary with temperature and compensate them with each other by subtracting or adding them, etc.

To allow ultra-low power consumption, the transistors used in the current reference circuit should operate in weak inversion (subthreshold) region. In the subthreshold region, the drain current can be calculated using equation 3.1

$$I_D = I_0 \exp^{\frac{V_{GS}}{V_T}} \tag{3.1}$$

where I_0 is proportional to W/L and V_T is equal to kT/q, k is Boltzmann constant and q is the electrical charge on an electron [1]. According to equation 3.1, CMOS transistors in a subthreshold region behave like bipolar transistors, thus V_{GS} is CTAT [67] (i.e. when temperature increases, V_{GS} decreases). In addition, we can obtain ΔV_{GS} as

$$\Delta V_{GS} = V_{GS1} - V_{GS2} \tag{3.2}$$

$$\Delta V_{GS} = V_T \ln \frac{nI_{D1}}{I_{01}} - V_T \ln \frac{I_{D2}}{I_{02}} \tag{3.3}$$

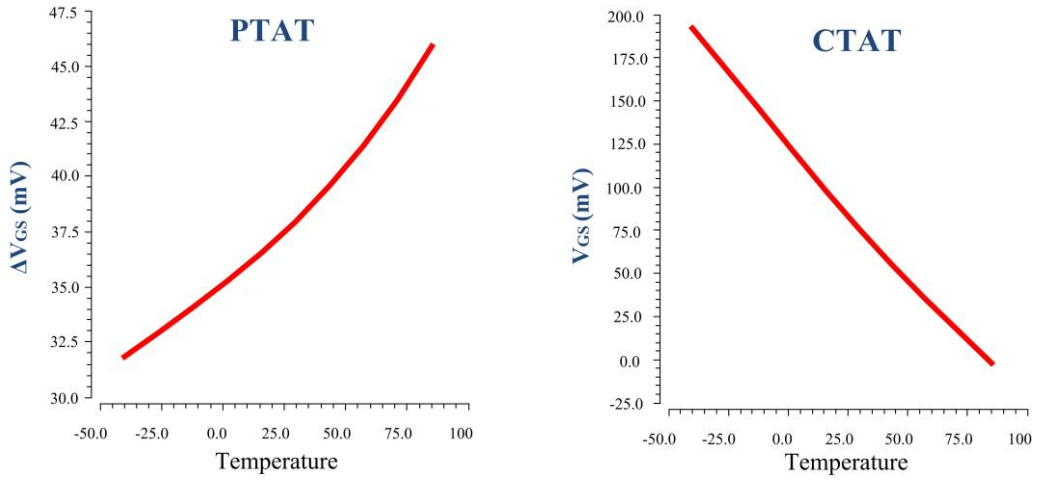

(a) (b)

Figure 3.2 ΔV_{GS} (a) and V_{GS} (b) variations of a CMOS transistor with temperature

If two identical transistors ($I_{01} = I_{02}$) are biased at drain currents of nI_D and I_D, we can write

$$\Delta V_{GS} = V_T \ln n \qquad 3.4$$

Thus, ΔV_{GS} exhibits a positive temperature coefficient, PTAT:

$$\frac{\partial \Delta VGS}{\partial T} = \frac{K}{q} \ln n \qquad 3.5$$

Interestingly, this temperature coefficient is independent of the temperature and the behavior of the drain current [67]. The simulated changes of ΔV_{GS} and V_{GS} of a CMOS transistor versus temperature are shown in Figure 3.2 (a) and Figure 3.2 (b), respectively.

Figure 3.3 shows the transistor level implementation of a current reference circuit. A start-up circuit is needed for the current reference circuit, because this circuit has two stable DC operating points. One of them is zero output voltage, so a start-up circuit is needed to guarantee that the reference circuit will not be working at its zero DC operating point. Once the circuit is pulled out of this zero DC operating point, the start-up circuit is disconnected to reduce power consumption.

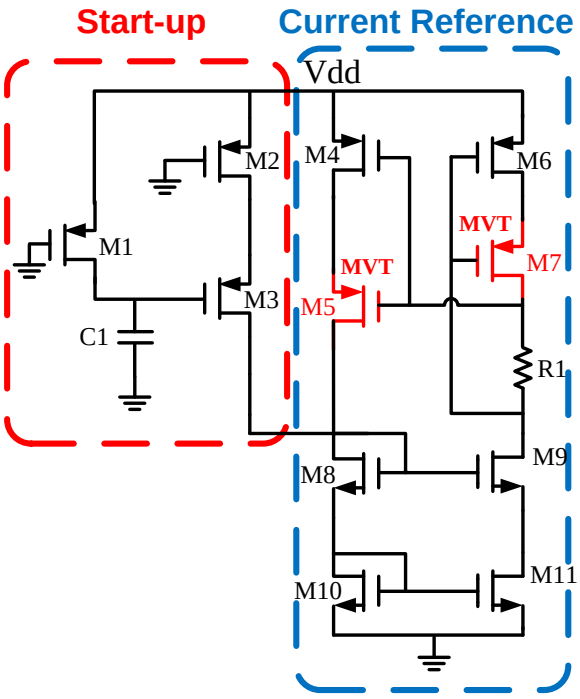

Figure 3.3 Circuit diagram of the proposed current reference generator.

The start-up circuit shown in Figure 3.3 consists of three PMOS transistors, M1, M2, M3, and a capacitor C1. At first, transistors M1 and M2 are ON because the gate of these two transistors are connected to the ground and transistor M3 is also ON, because the capacitor C1 is not charged yet. After charging the capacitor through transistor M1, M3 turns OFF and the start-up circuit disconnects itself.

A current reference circuit is utilized to provide a constant current to the oscillator circuit to control the power consumption of the oscillator. According to Figure 3.3, it consists of eight MOS transistors M4-M11 and one N-well resistor, R1. Based on circuit simulations, this circuit consumes only 32 nW from its 1 V supply, which is suitable for ultra-low power applications.

In this circuit, R1 is inserted between the gates of transistors M4 and M6. Thus, the bulks and the sources of these two PMOS transistors can easily be connected to the voltage supply to avoid body effects. In addition, an extra branch is needed to bias the drain-source voltage of the PMOS

transistors for biasing a circuit at the voltage, which is needed for the desired current, which is planned for. In this current reference, medium-threshold voltage (MVT) transistors have been used to implement transistors M5 and M7 to make a self-biased circuit for removing the extra branches, and as a result, reducing power consumption.

By performing a KVL on the loop including transistors M4 and M5 (M6 and M7), drain-source voltages of M4 and M6 can be expressed as:

$$V_{DS\text{-}M4,6} = V_{GS\text{-}M4,6} - V_{GS\text{-}M5,7} \quad 3.6$$

Difference of two gate-source voltages of transistors M4 and M5 in the subthreshold region is almost proportional to the difference of their threshold voltages [1] which is the difference between the regular threshold voltage and medium threshold voltage in this technology.

The main idea of this strategy is to bias this circuit at the point where the reference current is less sensitive to temperature variations. In this design, all transistors are biased in their weak inversion region. The voltage across resistor R1 can be written as:

$$I_D = I_0 \, exp^{\frac{V_{GS}}{V_T}} \quad 3.7$$

$$V_{GS4} = V_T \ln \frac{I_{D4}}{I_0} \quad 3.8$$

$$V_{GS4} = V_T \ln \frac{I_{D6}}{I_0} \quad 3.9$$

$$V_{R1} = V_{GS\text{-}M6} - V_{GS\text{-}M4} \quad 3.10$$

$$= V_T \ln \frac{I_{D-M6}}{I_0} - V_T \ln \frac{I_{D-M4}}{I_0} \quad 3.11$$

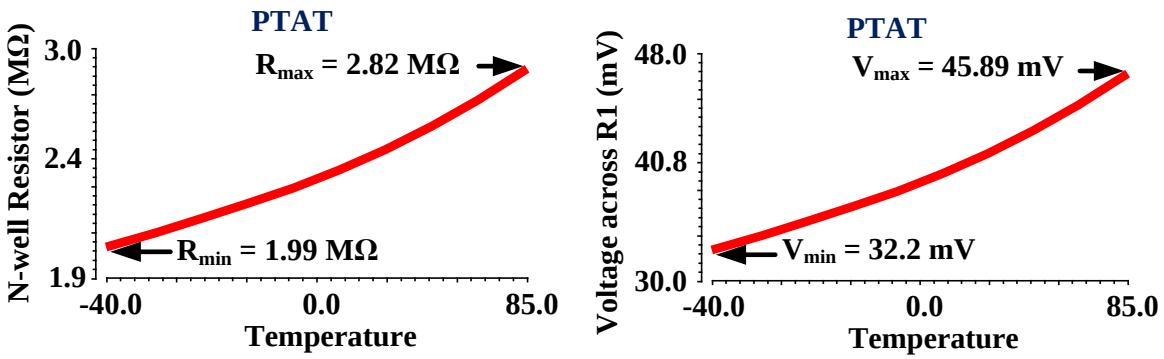

(a) (b)

Figure 3.4 Variations with temperature of (a) N-well resistance, and (b) the voltage across resistor R1 in the current reference

According to the above equations, the difference of two gate-source voltages in the subthreshold region is proportional to the thermal voltage (V_T). As depicted in Figure 3.4 (a) a N-well resistor is PTAT. Thus, the voltage across the N-well resistor (V_{R1}) is also PTAT. The current flowing through R1 can be written as:

$$I_{Ref} = \frac{V_{R1}}{R_1} \qquad 3.12$$

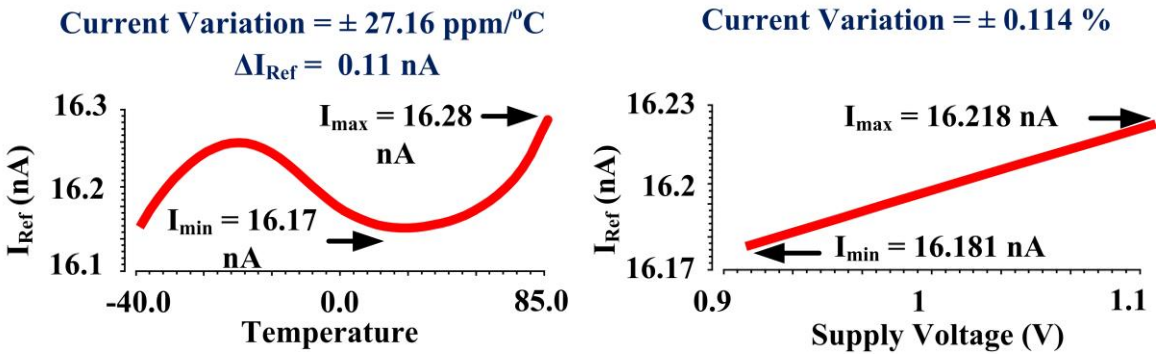

(a) (b).

Figure 3.5 Reference current as a function of (a) Temperature variation and (b) Supply voltage variation.

Since V_{R1} is PTAT and the N-well resistor is also PTAT, a proper biasing level allows the effects of these two PTATs to be compensated (by equalizing the values of their slopes) and the current at that biasing point is almost independent of temperature variations.

The voltage across the N-well resistor in the current reference versus temperature variation is plotted in Figure 3.4 (b), and according to Figure 3.4(a) and Figure 3.4(b), they both increase with temperature and they are PTAT, so the effect of these two PTATs can compensate each other when the voltage across the resistor is divided by the resistor value and the current becomes almost independent to temperature variations. Moreover, the generated reference current versus temperature is plotted in Figure 3.5 (a), where it deviates only 0.34% from its nominal value (16.2 nA) over a temperature range between -40 and 85 °C. In addition, the reference current as a function of the supply voltage variation is plotted in Figure 3.5 (b). The current shows only 0.114% variation over ±10% variation in the supply voltage, so the supply voltage variation has a negligible effect on the total current consumption of the system. The performance of the current reference circuit is summarized and compared with similar designs in Table 3.1. As shown in this table, our presented design achieves a good performance when compared to other cited designs in terms of the power consumption and current variation with the temperature.

Table 3.1 Performance summary and comparison of the proposed current reference.

Reference	[83] (simulated)	[84] (simulated)	[73] (simulated)	[85] (simulated)	[86]	This work (simulated)
CMOS Technology (µm)	0.35	0.09	0.18	0.35	0.18	0.18
Temperature Range(°C)	-20 to 80	0 to -70	-30 to 135	-20 to 60	-40 to 100	-40 to 85
Supply Voltage (V)	1.2	0.5	2.4	1.1	1.8	1
Power Consumption (µW)	0.073	0.234	24	0.054	3	0.031
Current Variation (ppm/ºC)	± 335	476	57	± 212	577	± 30

This current reference has three main features: first, it consumes very low power, only 32nW, which is suitable for the proposed sensor. Secondly, it is of interest that it has a minimum number of branches, for typical bandgap circuits usually comprise at least three branches. The last main point is the low dependency to temperature and supply voltage, which are plotted in Figure 3.6 (a) and 3.6 (b), respectively.

3.2 Oscillator

Oscillators are used in many analog circuits and they are a part of many systems, such as clock generation in analog to digital converters (ADCs) and microprocessors.

Oscillation can result of ill designed feedback in a amplifier [1]. An amplifier with negative feedback is shown in Figure 3.6, and its transfer function can be calculated as

$$\frac{Vout}{Vin}(s) = \frac{H(s)}{1 + H(s)} \qquad 3.13$$

We have oscillation if the loop gain of the negative feedback system meets two conditions [1]:

$$|H(j\omega_0)| \geq 1$$

$$\angle H(j\omega_0) = 180^o$$

When designing an oscillator, we typically choose the loop gain to be two or three times that required for having oscillation in presence of the process and temperature variations. Two main classes of oscillator architecture can be considered in our system to generate the required clock

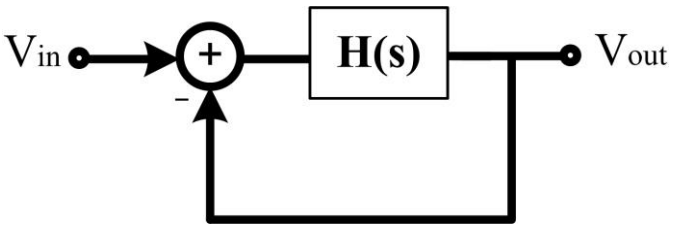

Figure 3.6 Amplifier with the feedback

signal: LC oscillators and ring oscillators. Although LC oscillators provide linear and stable performance, especially at low frequency, they consume high power compared to ring oscillators. In addition, LC-oscillators occupy large silicon area to implement inductors and capacitors. On the other hand, ring oscillators achieve lower power consumption and typically occupy a small silicon area.

3.2.1 Ring Oscillator

Since power consumption is very important in our application, we can start from the single stage inverter with feedback that consumes minimum power because it has only one stage. Unfortunately, this circuit is not oscillating because it has only one pole. So, we need at least two stages providing

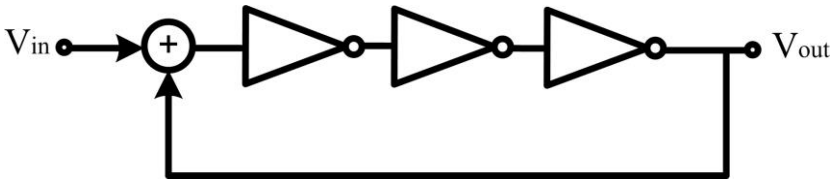

Figure 3.7 Three-stage ring oscillator

at least two poles to get a 180º phase shift. Unfortunately, from the standpoint of oscillator design, this circuit behaves as a bistable latch and does not oscillate.

As shown in Figure 3.7, a three-stage ring oscillator is used in this work. It allows low-power consumption and low area. The transfer function of the three-stage ring oscillator can be written as:

$$\frac{Vout}{Vin}(s) = \frac{\dfrac{-A^3}{\left(1+\dfrac{s}{j\omega_0}\right)^3}}{1-\dfrac{-A^3}{\left(1+\dfrac{s}{j\omega_0}\right)^3}} \qquad 3.14$$

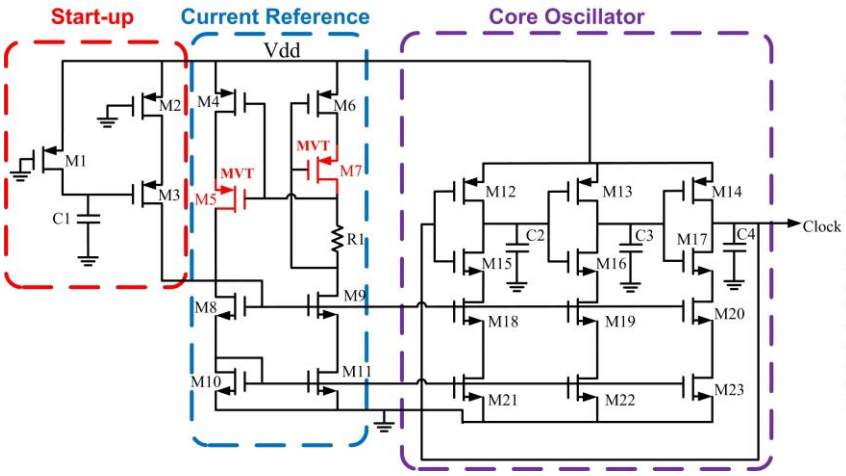

Component	Value
M1	W/L = 220nm/4µm
M2	W/L = 220nm/15µm
M3	W/L = 220nm/10µm
M4	W/L = 1µm/2µm
M5	W/L = 2µm/350nm
M6	W/L = 10µm/10µm
M7	W/L = 10µm/350nm
M8-M9	W/L = 15µm/300nm
M10-M11	W/L = 2µm/500nm
M12-M14	W/L = 220n/19µm
M15-M17	W/L = 1µm/1µm
M18-M20	W/L = 15µm/300nm
M21-M23	W/L = 2µm/500nm
C1	112 fF
C2-C4	155 fF
R1	2.4 MΩ

Figure 3.8 Transistor-level implementation of the proposed low-power oscillator

$$= \frac{-A^3}{\left(1 + \frac{s}{j\omega_0}\right)^3 + A^3} \qquad 3.15$$

According to the above equation, we have three poles in our oscillator.

$$S_1 = (-A - 1)\,\omega_0 \qquad 3.16$$

$$S_{1,2} = \left[\frac{A(1 \pm j\sqrt{3})}{2} - 1\right]\omega_0 \qquad 3.17$$

Considering that we have one T_D delay for each inverter, the loop delay that defines the period is $6T_D$. Thus, the oscillation starts at a frequency that can be calculated from equation 3.15 and then grows until the frequency shifts to $1/(6T_D)$ [1]. Figure 3.8 shows the schematic of the proposed 3-stage ring oscillator topology. It consists of three main circuits labeled: start-up, current reference,

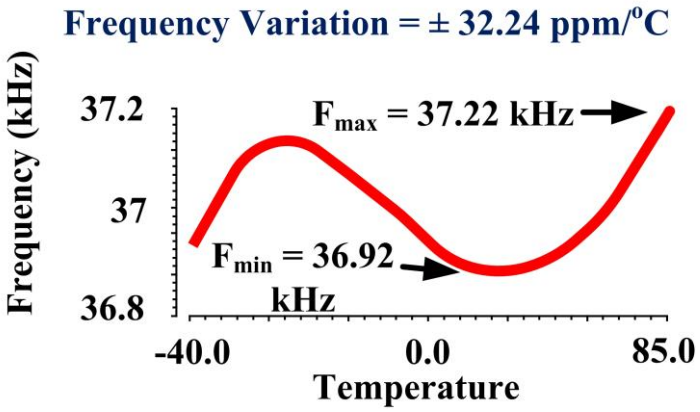

Figure 3.9 Oscillation frequency as a function of temperature

and core oscillator. The start-up and current reference circuits were described in the previous section.

A three-stage ring oscillator circuit has been implemented for the core oscillator part, where each stage is loaded by a 155 fF capacitor to increase the delay (T_D) for each stage and allow low-frequency operation. In this design, the current is mirrored from the bottom side (NMOS transistors) and variations in the frequency with temperature, which are shown in Figure 3.9,

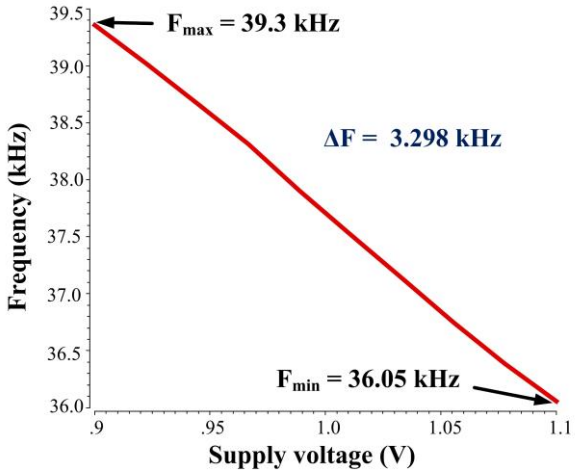

Figure 3.10 Oscillation frequency as a function of supply voltage variation

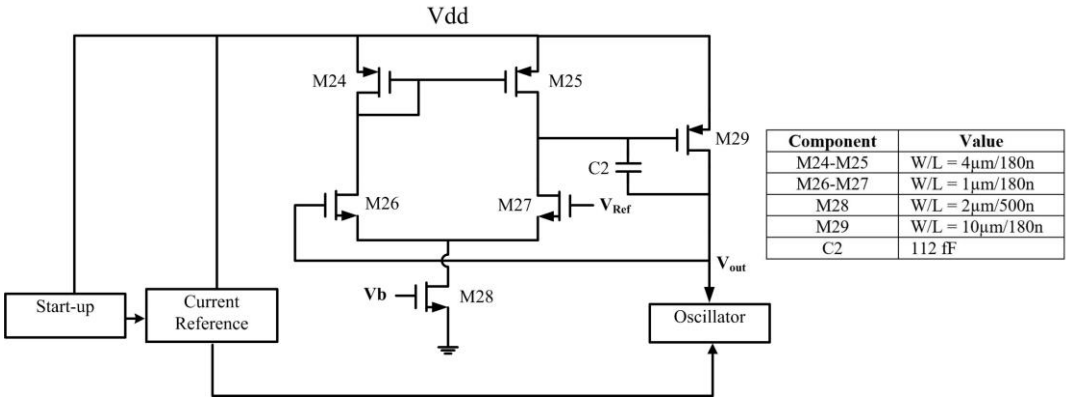

Component	Value
M24-M25	W/L = 4µm/180n
M26-M27	W/L = 1µm/180n
M28	W/L = 2µm/500n
M29	W/L = 10µm/180n
C2	112 fF

Figure 3.11 Oscillator with a regulation circuit

follow the current that is provided from the reference circuit because that current is forced to the core oscillator block.

However, the oscillation frequency of the circuit which is shown in Figure 3.8 is dependent to the supply voltage variation. According to Figure 3.10, it is 4.37% variation from its nominal with ±10% variation in the supply voltage. Power consumption of the proposed oscillator for different process corner cases is shown in Table 3.2.

One possible solution to reduce the impact of supply voltage variations on the oscillation frequency (supply rejection ratio and line sensitivity) is the use of a high-gain amplifier (two-stage amplifier) with negative feedback as shown in Figure 3.11.

Table 3.2 Power consumption of the proposed oscillator for different process corners

Corner	TT	FF	SS
Power Consumption (nW)	58	89	42

Supply variations can be compensated by the loop gain of the negative feedback. As shown in Figure 3.12, the simulated variation in the generated oscillation frequency due to ±10% changes in supply voltage is 0.19%. To increase the loop gain, a two-stage amplifier is designed. Moreover, a miller capacitor C2 is used to enhance the stability of the circuit and, to choose the value of this capacitor, a phase margin of 45 degrees is considered. Thus, the unity gain is chosen to be exactly below the second pole (ω_{p1}), which is at the output of the first stage. The value is transconductance of the first stage (gm_{M27}) over the total capacitor, which can be seen at that node that consists of the parasitic capacitors (Cpar) at that node, plus miller capacitor C2, multiplied by the one plus the gain of the second stage, which is transconductance of transistor M29 multiplied by the output impedance.

$$\omega_{p1} = \frac{gm_{M27}}{(1+gm_{M29} R0)\, C2 + Cpar} \qquad 3.18$$

This can be seen at the core oscillator, but the value of capacitor is chosen slightly more than that value for some margins. In this system, the two-stage amplifier is used to tune the oscillator output frequency. All employed MOS transistors are designed in a weak inversion to decrease the power consumption. At the first stage, an OTA (five transistor amplifier) is used, which is followed by common source stage in a negative feedback configuration.

As V_{Ref} (which can be generated by a bandgap circuit) rises, transistor M27 begins to draw current from M25, turning transistors M24 and M26 on. Note that, since $I_{D25} \approx I_{D24}$, we have $I_{D27} \approx I_{D26}$ and $V_{GS27} \approx V_{GS26}$. Therefore, $V_{out} \approx V_{Ref}$.

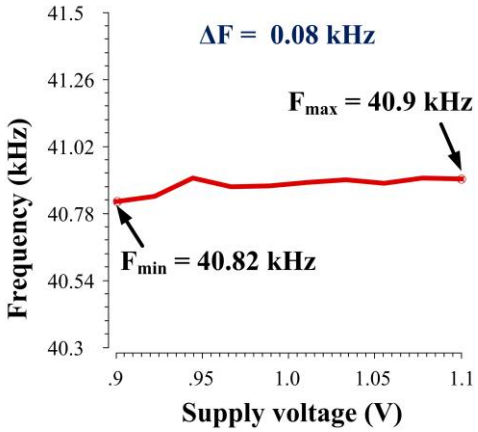

Figure 3.12 Oscillation frequency versus supply voltage changes

However, adding the two-stage amplifier to the oscillator circuit increases the power consumption from 58nW to 107.3nW. In addition, this oscillator is designed to be used in the proposed battery-less sensor, where the variation in the frequency with the supply voltage is not significant. Indeed, a shunt regulator is used to reduce sensitivity and a small frequency variation has no significant effect on the sensor performance. Although the solution with a high-gain amplifier is not used, according to Figure 3.10, frequency changes only by ± 4.3% over ±10% variation in the supply voltage, which does not have an effect on the functionality of the proposed system.

Figure 3.13 Voltage-controlled oscillator (VCO)

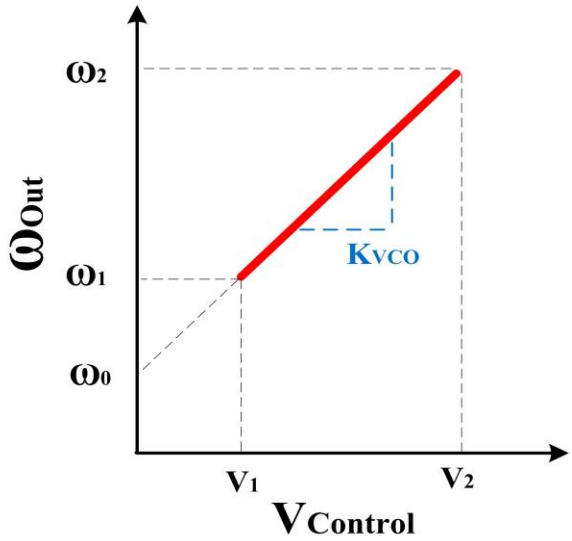

Figure 3.14 Frequency versus control voltage

It worth noting that the presented oscillator could be modified to a voltage-controlled oscillator (VCO) to generate a tunable oscillation frequency depicted in Figure 3.13. This VCO is needed for several applications such as phase-locked loops, frequency synthesizers, etc.

The output frequency of an ideal VCO is a linear function of its control voltage, as shown in Figure 3.14 and the equation describing it can be written as

$$\omega_{Out} = \omega_0 + K_{VCO}\, V_{Control} \qquad 3.19$$

Where, K_{VCO} is defined as gain or sensitivity of the VCO (expressed in rad/s/V) and also, tuning range can be defined as an achievable range in frequency (i.e. $\omega_2 - \omega_1$). The actual behavior of the VCO circuit exhibits nonlinearity (i.e. K_{VCO} is not constant across the tuning range) because of the nonlinear components that we have in the circuit. Thus, VCO's linearity could be improved with minimizing the variation of K_{VCO}. Supply rejection ratio or line sensitivity is another important factor in designing VCOs, especially if they are realized in a single-ended form [1].

To control the output voltage of the oscillator, one DC voltage is enough, but it is important that it does not stabilize at $(I \approx 0)$; it is common to use a source follower transistor as a buffer, but in

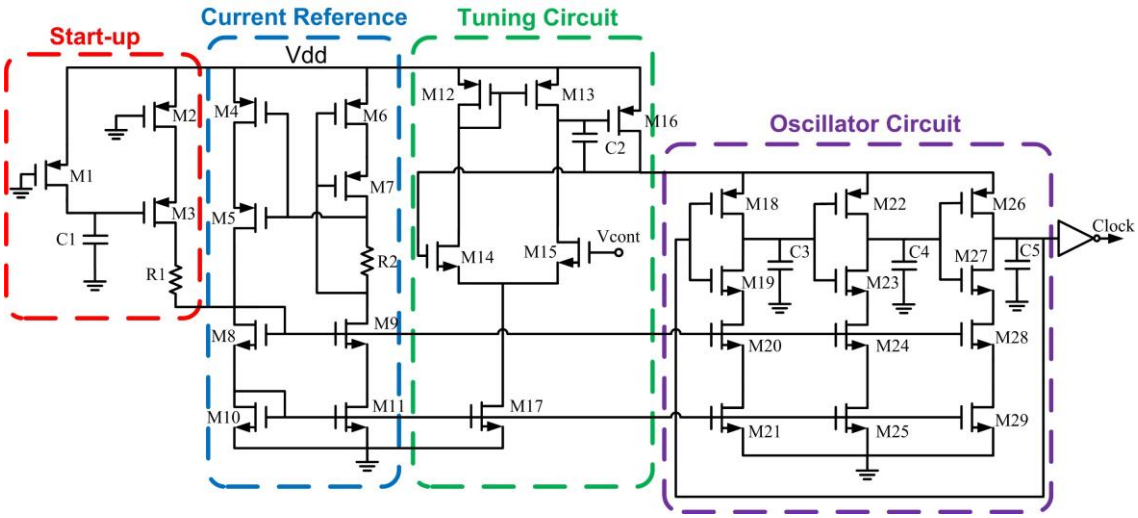

Figure 3.15 Transistor-level implementation of the proposed VCO

that way, because V_{GS} operates in subthreshold region and is CTAT (complementary to absolute temperature), its characteristics change with temperature. Therefore, one of the reasons to employ a two-stage amplifier is to reduce the effect of V_{GS} , which is CTAT with negative feedback. Figure 3.15 presents the schematic of the proposed VCO, where a two-stage amplifier oscillator. It is important that its characteristics be independent of temperature, which further is used to tune the oscillator's output frequency.

All MOS transistors used in this circuit are operated in weak inversion to decrease power consumption. At the first stage, an OTA (five transistor amplifier) is used followed by a common source stage in negative feedback configuration. This circuit is a well-known regulator configuration, one inverter is used at the end to reduce the transition time of the oscillator's output signal. It is worth noting that this inverter is supplied from the main supply voltage (V_{DD}), and thus, the output signal goes up to V_{DD} and is not limited by the upper voltage of the core oscillator, which changes while tuning the circuit.

The charge of capacitors can be expressed as:

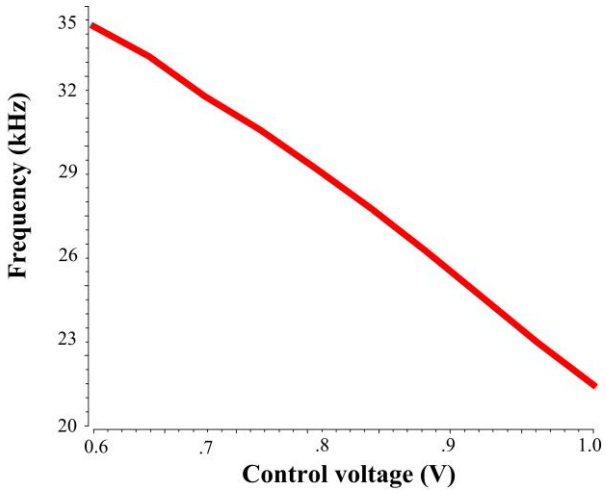

Figure 3.16 VCO output frequency versus its control voltage (Vcont)

$$Q = C\,V \tag{3.20}$$

$$I = C\frac{dv}{dt} \tag{3.21}$$

$$I = C \times \Delta V \times \Delta f \tag{3.22}$$

$$\Delta f = \frac{I}{C \times \Delta V} \tag{3.23}$$

According to the above equation and Figure 3.16, the current and the capacitor's values are constant, thus the frequency is proportional to the control voltage (Vcont). This means that if the voltage across the capacitor is increased, the frequency will decrease. Moreover, changes in VCO's power consumption with the output frequency is plotted in Figure 3.17. According to this Figure, power consumption is increased as frequency is reduced because the current is constant and if we have a larger voltage, it takes more time for discharging the capacitors.

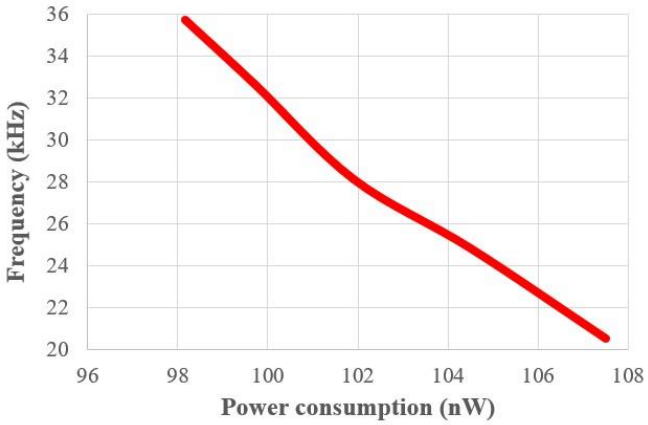

Figure 3.17 Changes in VCO's power consumption with increasing the output frequency

3.2.2 Post-layout simulation results

The proposed oscillator has been implemented using a 0.18 µm standard CMOS process. The layout view of the implemented oscillator is shown in Figure 3.18. Its implementation consumes 190 µm x 120 µm silicon area. Figure 3.19 shows the effect of the temperature variations on the

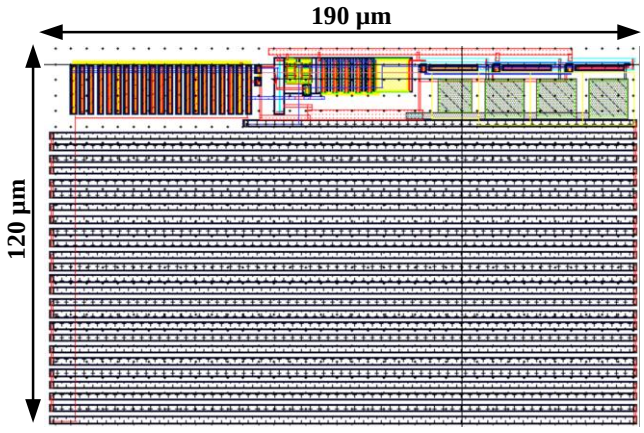

Figure 3.18 Layout view of the proposed oscillator

oscillation frequency. It is found that the generated frequency changes by only ± 0.43% from its 37.7 kHz nominal value, when temperature varies between -40 and 85 °C.

The implemented oscillator consumes only 58 nW from its 1 V supply. In addition, it shows a temperature coefficient of 70 ppm/°C (± 35 ppm/°C), which is suitable for the proposed low-power battery-less sensor node. The reference current variation in response to ±10% variation in supply voltage is plotted in Figure 3.20 (a), where the current deviates by only ±0.12% from its nominal (16.2 nA) value. Similarly, when temperature varies between -40 and 85 °C, Figure 3.20 (b) shows

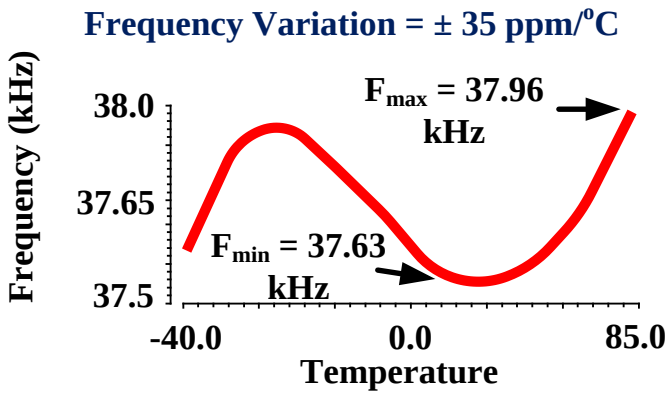

Figure 3.19 Output frequency as a function of temperature

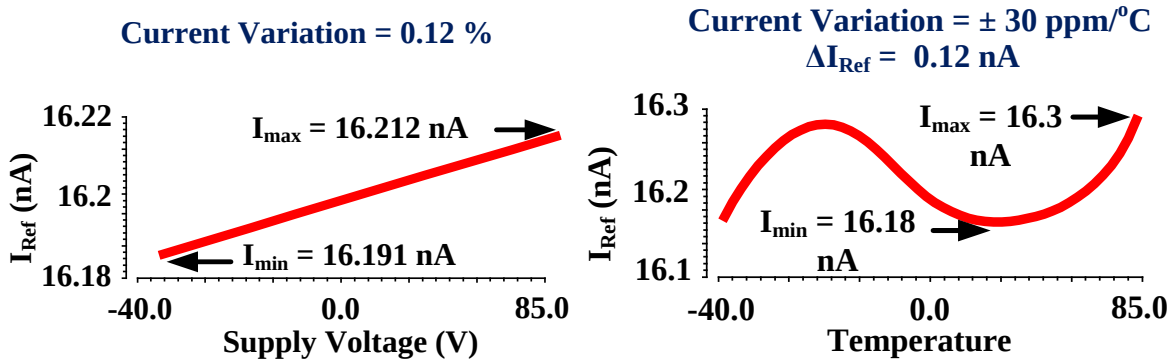

(a) (b)

Figure 3.20 Reference current as a function of (a) Temperature variation and (b) Supply voltage variation

Table 3.3 Performance summary and comparison of the proposed oscillator.

Reference	[87] (sim)	[88] (sim)	[89] (sim)	[90] (sim)	[76]	This work (simulated)
CMOS Technology (µm)	0.35	0.065	0.11	0.13	0.25	0.18
Temperature Range (°C)	0 to 80	-55 to 125	-20 to 80	-30 to 85	-20 to 80	-40 to 85
Supply Voltage (V)	1	0.6	1.2	1.2	0.8	1
Oscillation Frequency (kHz)	80	13800	20	40.2	6.4	37.7
Power Consumption (µW)	1.14	52.8	4.9	0.93	0.075	0.058
Frequency Variation (ppm/oC)	±421	±22.5	314	101	148	± 35
Area (mm2)	0.24	NA	NA	0.025	1.08	0.0228
FOM (nW/kHz)	14.2	3.82	245	23.13	11.71	1.5

that the current varies only 0.12 nA. It was also found that ±10% variation in the supply voltage has a negligible effect on the total current consumption of the system. Table 3.3 summarizes the performance of the proposed oscillator. This table shows that the proposed oscillator design achieves a good performance (power consumption, area and frequency variation with temperature) when compared to the state of the art. The figure of merit is defined as the power consumption divided by the oscillation frequency, and this work shows competitive performance compared to the other reported works.

3.3 Tuning block

Figure 3.21 shows the tuning loop which is designed to set a proposed system at its resonance frequency to achieve maximum power delivery. According to Figure 3.22, this loop exploits a peak detector, a counter, a block for binary code to thermometer code conversion, and a digital to analog

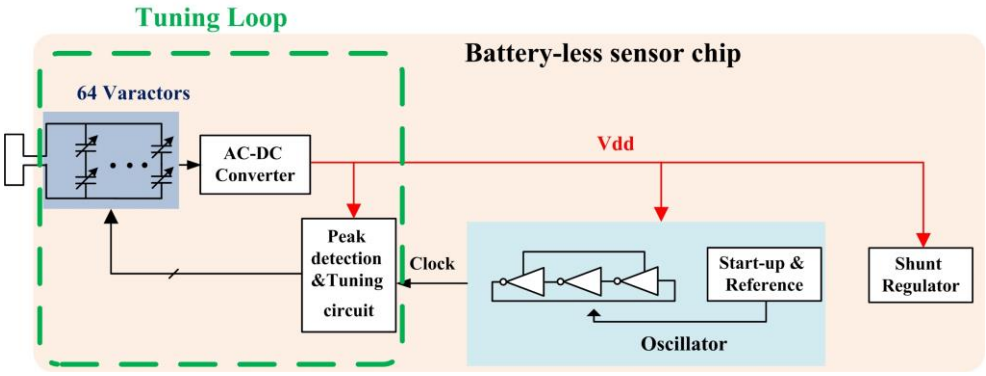

Figure 3.21 The proposed system

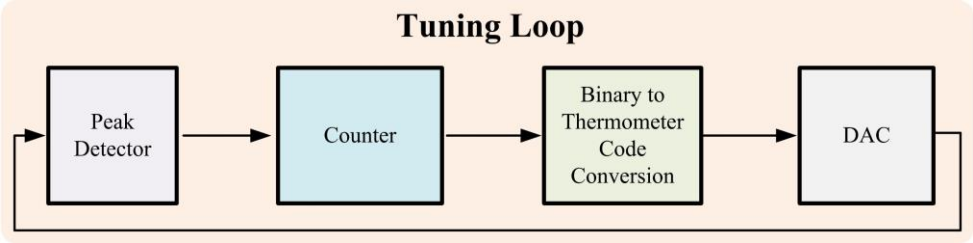

Figure 3.22 Tuning loop

converter (DAC). The peak detector circuit is used to monitor the generated voltage from the AC-DC converter and to control the counter upward or downward. This information can be used to tune the matching network, until the voltage provided from the AC-DC converter reaches its peak. The binary code generated from the counter, when the loop settles, reflects the state of the environment.

3.3.1 Digital to Analog Converter

this block converts the digital input (A_{in}) to an analog output (V_{out}) through an analog reference (V_{Ref}), which is shown in Figure 3.23. The relationship between these three signals can be written as:

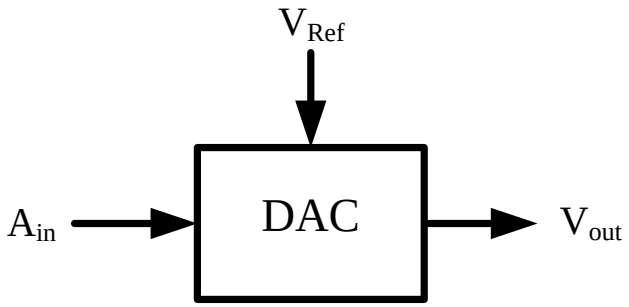

Figure 3.23 Digital to analog converter (DAC)

$$V_{out} = V_{Ref} \times (A_1 2^{-1} + A_2 2^{-2} + \ldots + A_n 2^{-n}) \qquad 3.24$$

Where n represents the number of bits that DAC is designed for.

In all of the data converters, there are two fundamental errors, the Integral Nonlinearity (INL) and the Differential Nonlinearity (DNL)[77]. The transfer function of an ideal data converter is a straight line and deviation from that line after both the offset and gain errors have been removed can be defined as INL error. In addition, each step size in an ideal data converter is equal to 1 LSB and 1 LSB is defined as:

$$1 \text{ LSB} = \frac{V_{Ref}}{2^n} \qquad 3.25$$

The variation in analog step size away from 1 LSB when gain and offset errors have been removed can be defined as DNL. Also, we can define the monotonicity of the data converter as the output that always increases as the input is increased, which means that the slope of the transfer function of the data converter has only one sign. If the maximum DNL error is less than 1 LSB or the maximum INL error is less than 0.5 LSB, a converter is guaranteed to be monotonic [53]. Different types of the DACs exist such as R-2R-based DAC and capacitive DAC. Each one has its own benefits; for example, capacitive DAC has a better Integral nonlinearity (INL) error [78], so they have their own applications.

Switches can have a large series ON resistance that increase power consumption. In this work, varactors are chosen because they have a lower series resistance compared to switches.

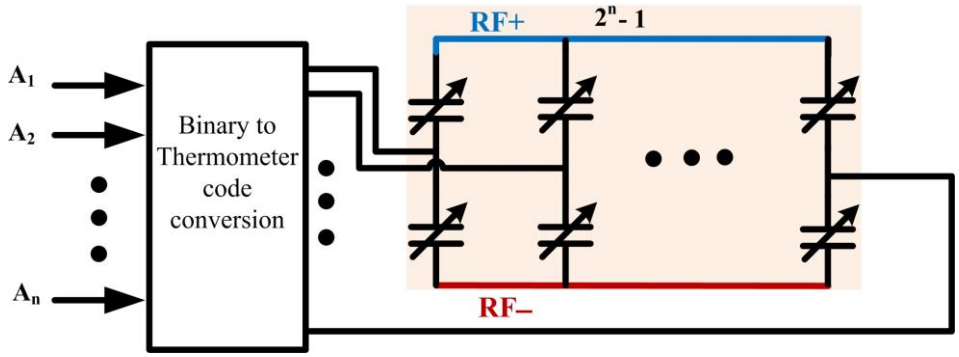

Figure 3.24 Controlling varactors for delivering maximum power

3.3.2 Varactor Designs

Figure 3.24 would be a good choice for this application because there are only two terminals after the antenna (RF+ and RF-) and there is no ground or virtual ground. The DC voltage at these two terminals are half of the final DC value [50], which is 0.5V in our work.

According to Figure 3.24, two varactors are used in series and the upper plate of the top varactor is connected to the RF+ terminal and the same plate of the other varactor is connected to the RF- terminal. In addition, the voltage between them is set by a binary to thermometer converter block

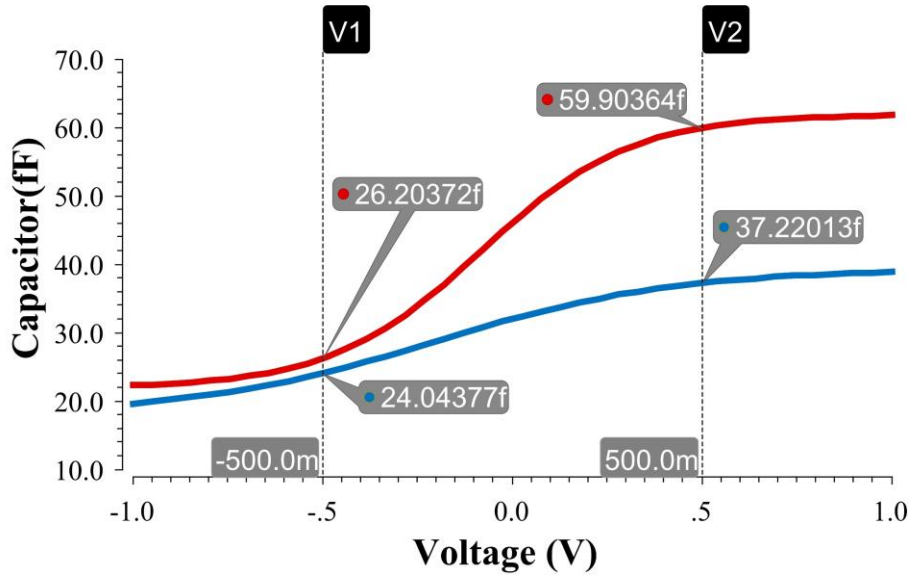

Figure 3.25 Capacitance tuning range of the two varactors available in the 0.18 μm CMOS process

and as a result the value of the varactor is changed. So, identical units of the varactors can be used. By changing the voltage at the middle point of two varactors that this voltage comes from a binary to thermometer code conversion, the total capacitance can be determined. We can change it until receiving the maximum power, which is detected by the peak detector. Then, the capacitance is monitored, which indicates the variation in the environment parameter to be measured. For 5-bit resolution, we need 62 units of the varactors. When selecting the varactor, the important thing is the capacitance tuning range. In the 0.18 µm CMOS process, only two varactors are offered. They can be simulated as shown in Figure 3.25. According to this figure, the varactor response shown in red has a wider capacitance tuning range over the performance shown in blue.

3.3.3 Counter

A counter is a fundamental and important block in a digital system. Counters have many applications, such as timing operations, controlling other blocks, and use as a frequency divider. Figure 3.26 shows the logic diagram of the employed synchronous counter [79]. This counter comprises five flip flops, because our sensor is designed for 5-bit resolution. To reduce the settling time and to be closer to the ideal setting of the matching network, it was decided to start the counter from its mid-range value. Therefore, the counter starts from the “10000” binary code.

One of the other issues that must be considered is whether the peak detector will send the upward command when the counter reaches its peak. In a classical counter, it will continue from the bottom

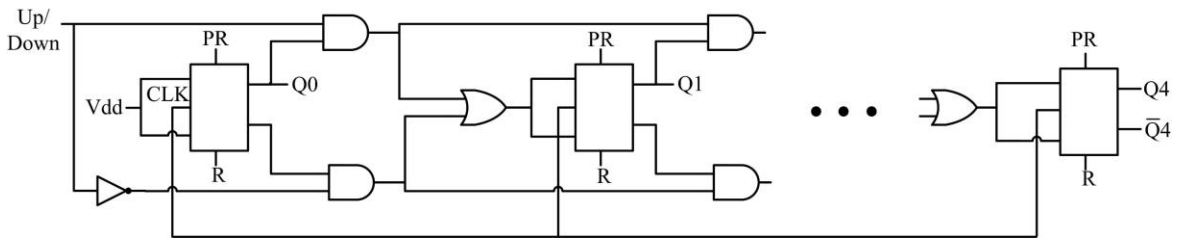

Figure 3.26 Controlling varactors for delivering maximum power

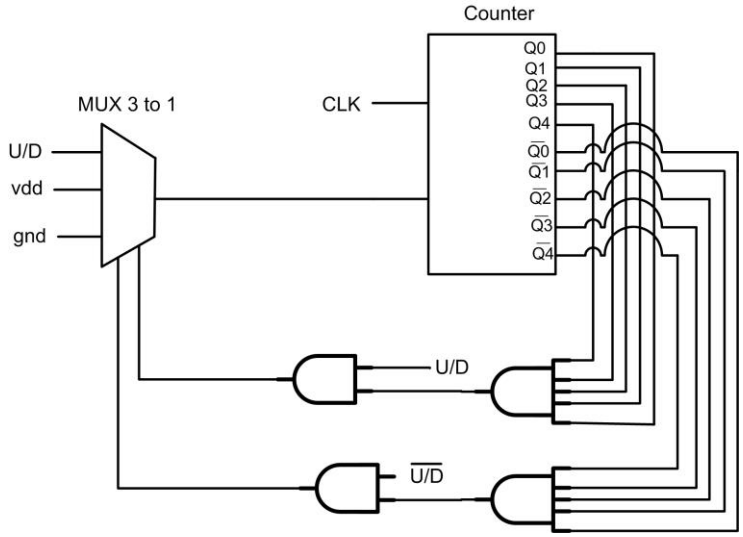

Figure 3.27 Freezing counter structure.

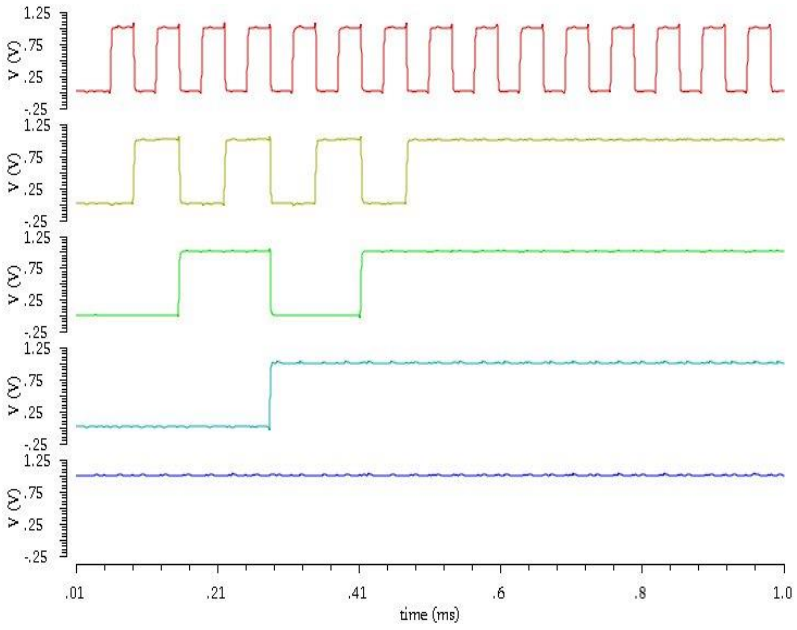

Figure 3.28 Output waveforms of the counter

side. Also, when the counter reaches its minimum value and receives the downward command, it will continue counting from the top. To solve this issue, the circuit, which is shown in Figure 3.27,

is designed. As a result, when the peak detector sends the upward command to the counter, the counter sees the downward command and starts ringing between the maximum state and the state just before the counter reaches its peak. For the downward counting, when it reaches the end, the peak detector sends the downward command, and the counter will see the upward command and start switching between the minimum state and the state before the minimum, which shows that the counter reaches its minimum value. In this case, we can state that the counter saturates either at its top or bottom value, but it is still functional for real-time sensing. Figure 3.28 shows the functionality of the counter circuit, which starts oscillating between its two maximum values.

3.3.4 Binary to Thermometer Code Converter

In a thermometer code, a value representing number N has the lowest N bits as “1”, and the other bits are set to “0”. So, to move from N to N+1, the rightmost “0” is just changed to “1”. Table 3.4 shows an example of 3-bit binary and thermometer codes.

The binary code, which is generated by the counter, is needed to convert to a thermometer code to control the varactors. With this technique, each time the value of one of the units of the varactors is changed until it reaches its settling value.The transient simulation and the logic diagram of the binary to thermometer code converter is shown in Figure 3.29 [80]. It worth noting that when the binary to thermometer code converter reaches its maximum value, which is T31, it starts ringing between T30 and T31, which indicates that the loop is settled. Since the proposed sensor is a real-time sensor, it must remain functional after reaching the maximum or the minimum values of the counter.

Table 3.4 bit binary and thermometer

Decimal	Binary Code			Thermometer Code						
	D_2	D_1	D_0	T_1	T_2	T_3	T_4	T_5	T_6	T_7
0	0	0	0	0	0	0	0	0	0	0
1	0	0	1	0	0	0	0	0	0	1
2	0	1	0	0	0	0	0	0	1	1
3	0	1	1	0	0	0	0	1	1	1
4	1	0	0	0	0	0	1	1	1	1
5	1	0	1	0	0	1	1	1	1	1
6	1	1	0	0	1	1	1	1	1	1
7	1	1	1	1	1	1	1	1	1	1

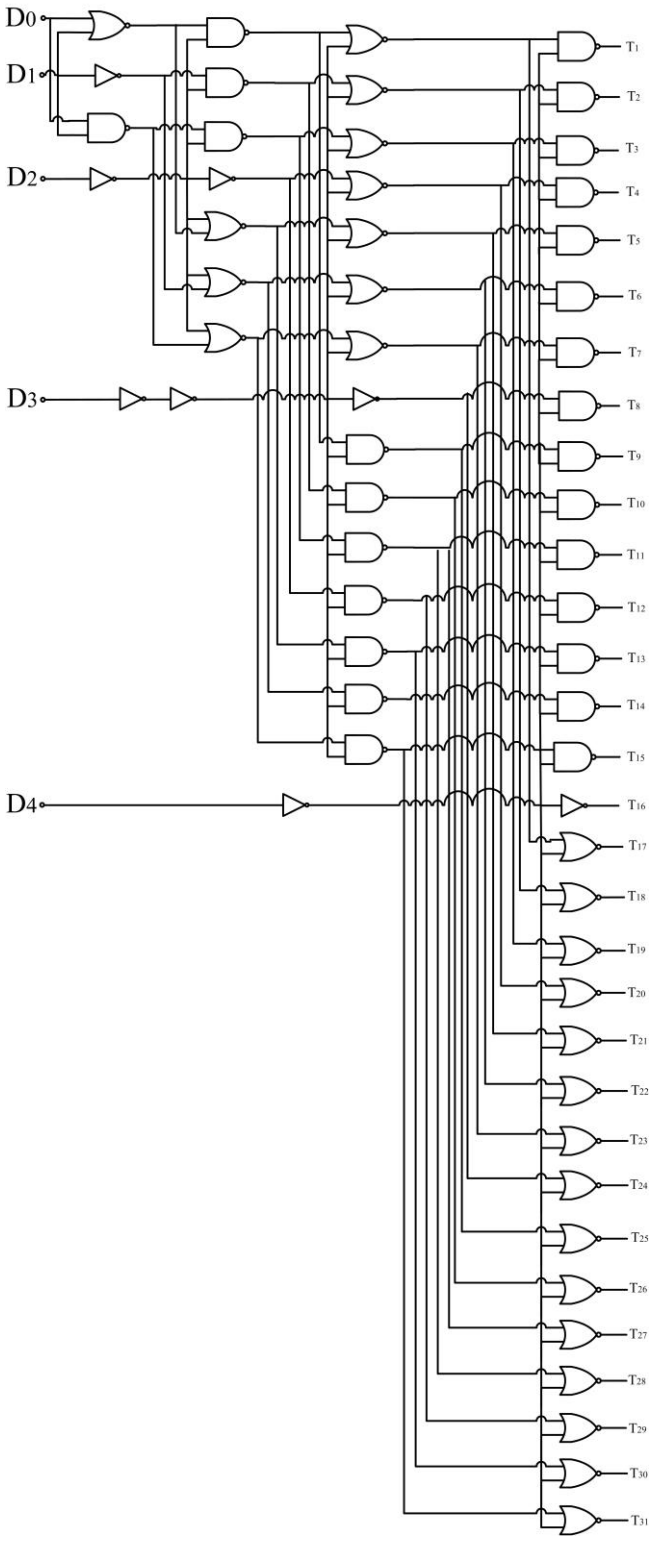

Figure 3.29 Logic diagram of the binary to thermometer code converter

3.3.5 Peak Detector

A peak detector circuit is used in the proposed battery-less sensor node to measure the peak of the signals. It shows the highest value of the waveform. A simple configuration of a peak detector uses a diode and a capacitor.

The diode (D1) conducts the positive half cycle of the input signal and the capacitor is charged to the peak of the signal. When the input signal goes below the peak value, the diode becomes a reversed bias and blocks the current from the capacitor to the source. The main limitation of this configuration is loading the input signal because the diode behaves as an instant switch. Therefore, designing one buffer before the diode is needed to avoid the loading effect, while the capacitor is charging during the positive half cycle of the input signal.

In ultra-low-power designs, it is very important to reduce complexity to reduce power consumption. Furthermore, in this work, a very accurate peak detector is not needed because we just need to design a circuit that can follow the changes in the peak of the signal. Figure 3.30 shows the schematic of the peak detector used in the proposed battery-less sensor node, where the RF signal is tracked by transistors M1 and M2, which are designed in a subthreshold region. They act as a

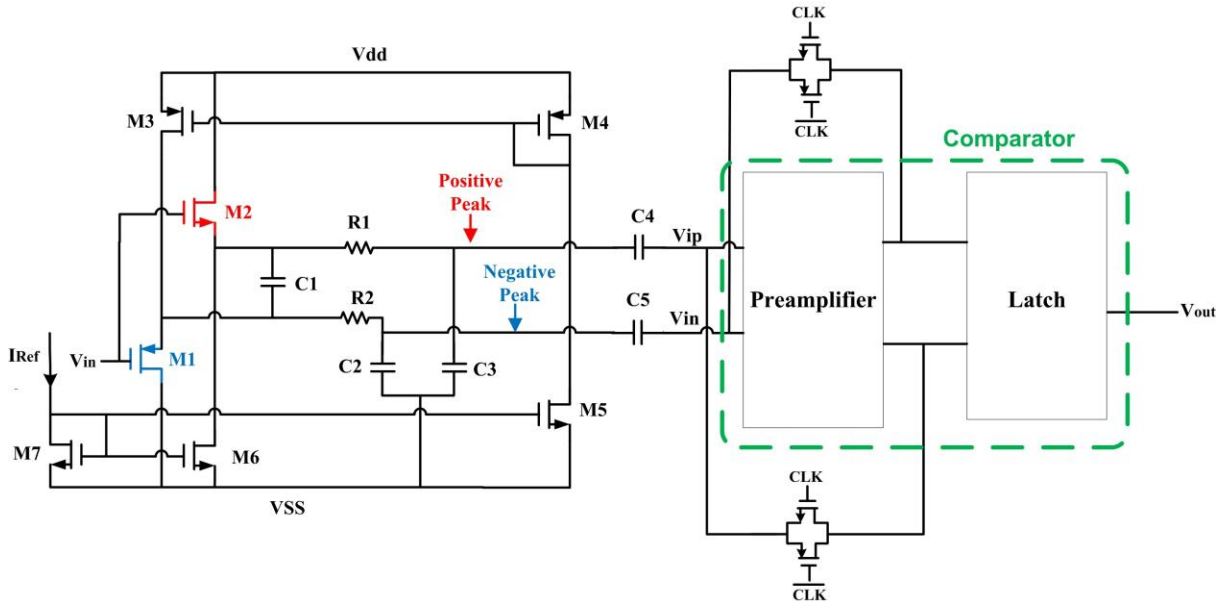

Figure 3.30 Transistor-level implementation of the proposed Peak detector

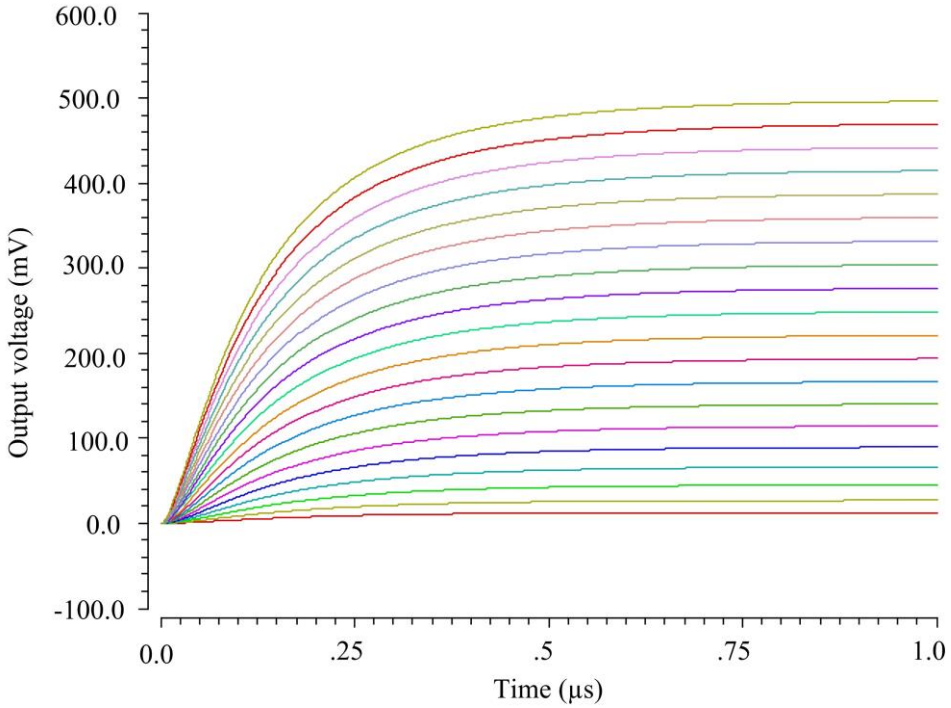

Figure 3.31 Output of the peak detector

source follower, so the source follows the voltage at their gate node until capacitor C1 charges to the peak value. Then, because the gate-source voltage becomes zero and even negative, the

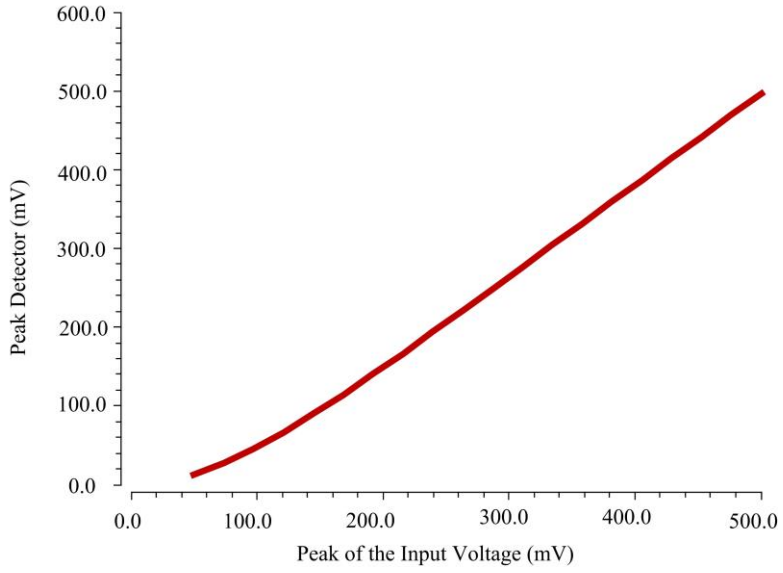

Figure 3.32 Peak detector voltage versus the peak of the input signal

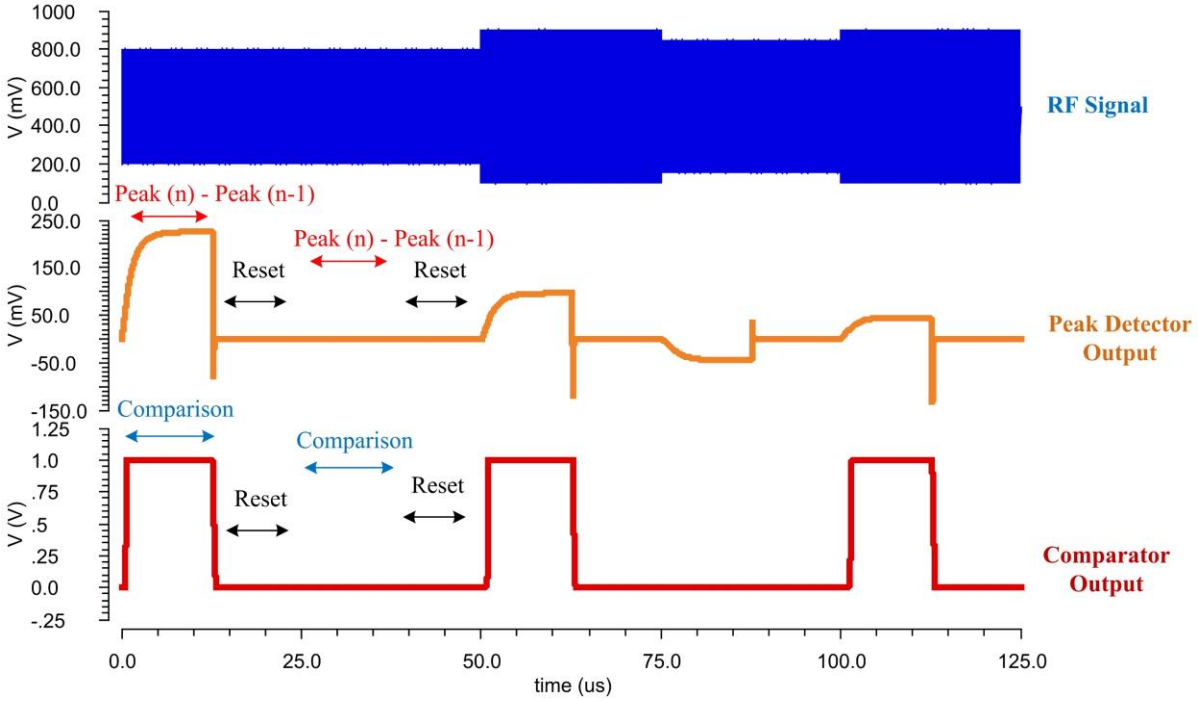

Figure 3.33 Output of the peak detector

transistors turn off and their source no longer follow the voltage at their gate. The PMOS transistor M1, detects the negative peak of the RF signal, while the positive peak is detected by the NMOS transistor M2. Thus, the voltage across the capacitor C1 is the peak-to-peak voltage of the RF signal. Then, the signal is filtered through the low-pass filter constructed by R1, C3, R2, and C2. We can then obtain a more constant and stable voltage signal, which is shown in Figure 3.31. The peak value, which is detected versus the input peak voltage, is shown in Figure 3.32 and this Figure presents, the proposed peak detector circuit can track the peak of the input signal. Strong arm comparator is used in this work and it consists of the two parts, a preamplifier, and a latch part [81]. A preamplifier is used to reduce the effect of the kickback error [77] and amplify the input signal. This amplified signal is then seen by a latch circuit. A differential common source topology with the diode connected transistor as a load is designed for this purpose. For an offset cancellation, complimentary switches which consist of a NMOS transistor, in parallel with a PMOS transistor, is used. Both must turn off at the same time,

and by selecting the appropriate aspect ratio (W/L) of the NMOS and PMOS switches, a channel charge injection error can be compensated [1]. Offset voltage is stored across the capacitor C4 and C5 during the reset phase and then the error is cancelled during the comparison phase. The latch circuit consists of two inverters that creates a positive feedback for regenerating the analog signal to the full-scale digital signal.

The functionality of the proposed peak detector and the comparator is shown in Figure 3.33. When the amplitude of the RF signal is changed, the peak detector, detects that and the comparator, compare the peak with the older ones and the output of that is shown in Figure 3.33.

3.4 Shunt Regulator

A voltage regulator is used to regulate the voltage levels in the proposed sensor and the resistance of the regulator changes, with both the input voltage and the load. Therefore, regulating block is acting like a variable resistance to adjust the output voltage. Two types of voltage regulator exist; a voltage regulator may be in parallel with the load (shunt regulator) or may be between the source and the load in a series (series regulator).

A shunt regulator provides a path from the supply voltage to the ground with a variable resistor, which is in parallel with the load of the circuit. Compared to series regulators, it is simpler and suitable for low-power circuits, because the dissipated current is too small.

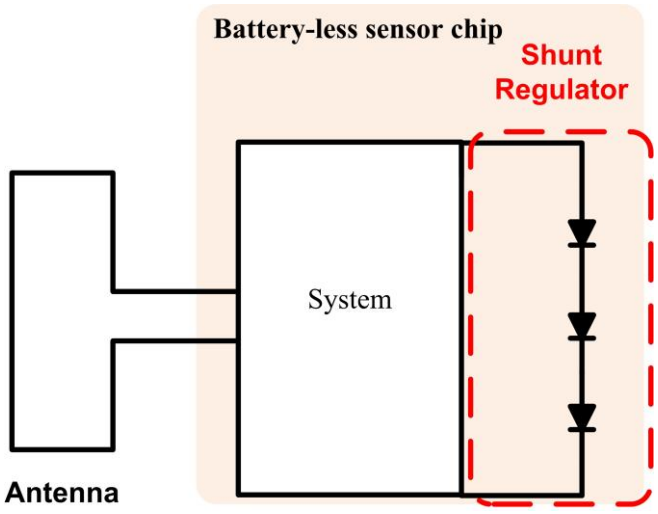

Figure 3.34 Shunt regulator

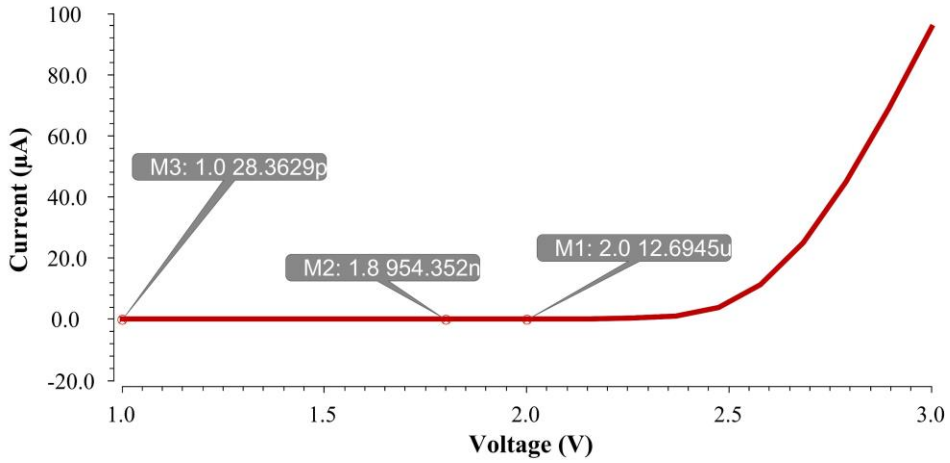

Figure 3.35 Voltage versus current

In the proposed wireless battery-less sensor because RF energy harvesting is used for the energy source, it can provide different voltages, which is dependent on the distance from the source of the energy. Therefore, a circuit needs to be designed to protect the system. This block does not need to be very accurate; the purpose of this block is only to provide protection to the proposed sensor.

As shown in Figure 34, three diodes in series configuration are used in parallel with the system to provide the required protection. This design is simulated in Fig. 3.35.

According to Figure 3.35, when the voltage is 1V, the current, which is consumed by the shunt regulator, is 28.36 pA. By increasing the voltage, the current increases, and because the power delivery is limited by the RF source, the voltage starts to drop. It can protect the system for a higher voltage level. It is shown that at the voltage value of 1.8 V, the current grows to 954 nA, and at 2V, the current goes to 12.69 µA, which is higher than the capacity of the RF source. As a result, the voltage starts to drop.

3.5 Simulation Results

Circuit-level simulations of the proposed system are presented in this section.

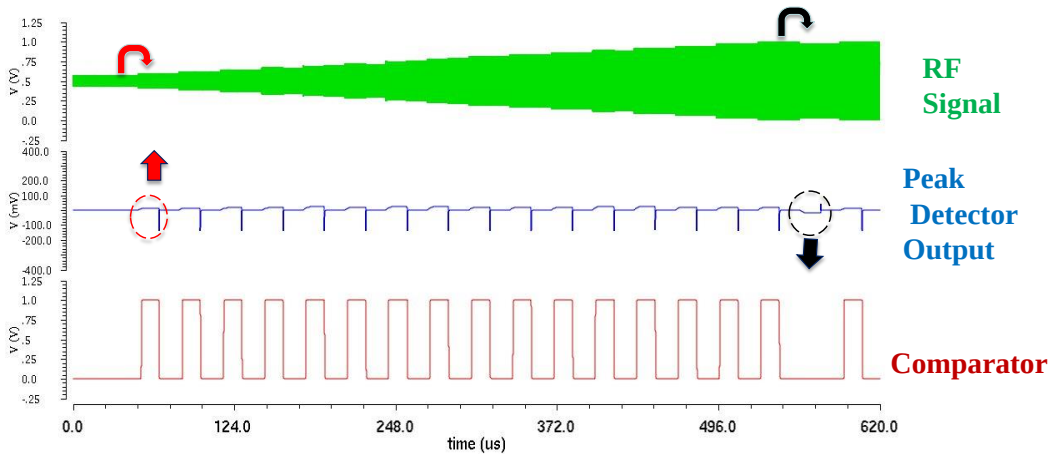

Figure 3.36 Output waveforms of the peak detector

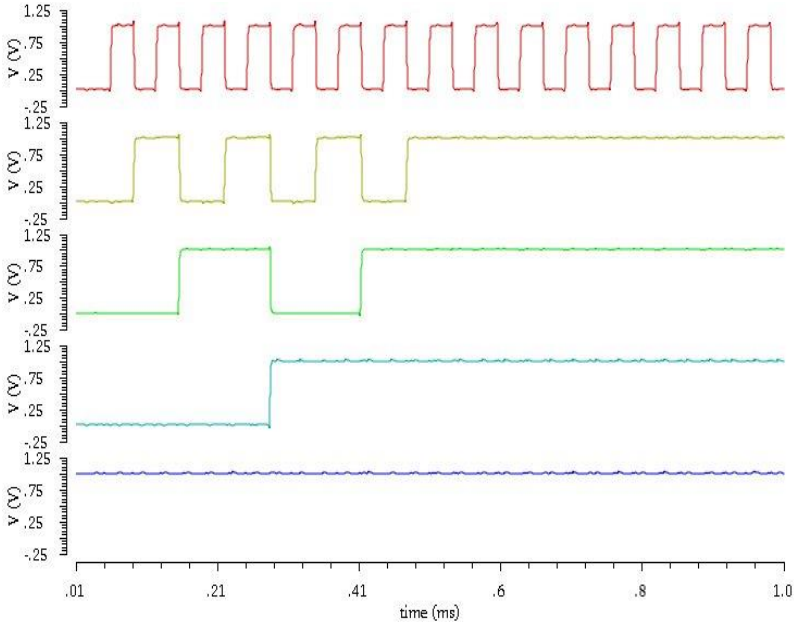

Figure 3.37 Output waveforms of the counter

Figure 3.36 shows the performance of the peak detector, comparator, and oscillator. The peak detector sends the upward signal to the counter until the amplitude of the RF signal is reduced and the peak detector detects that condition before sending a downward signal to the counter. The binary code which is generated from the counter is depicted in Figure 3.37, then this code is converted to a thermometer code as shown in Figure 3.38

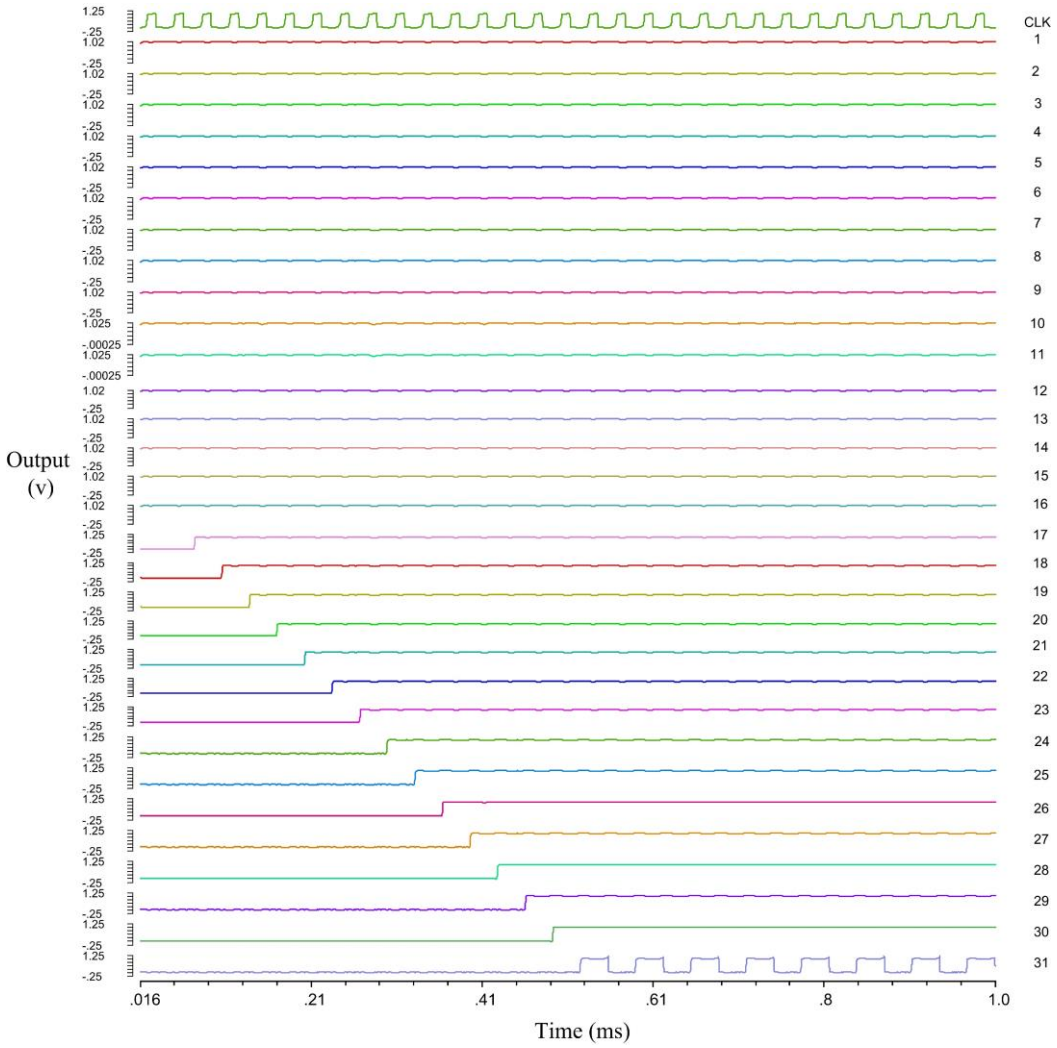

Figure 3.38 Transient simulation of the binary to thermometer code converter

Less complexity and merging the circuits with each other for achieving the minimum blocks are considered in all the circuits in this chapter for achieving a lower power consumption in compared to the state of the art [55].

CHAPTER 4 CONCLUSION AND FUTURE WORK RECOMMANDATIONS

4.1 Summary

An integrated wireless battery-less sensor was proposed in this thesis. The main idea of the proposed sensor is to sense environmental changes such as humidity through an antenna and a tuning technique. The main concept of this system is completely analyzed and investigated. In addition, the essential blocks needed to implement the proposed system are designed to obtain a very low power consumption.

The proposed sensor consists of five blocks: an AC-DC converter, a current reference, an oscillator, shunt regulator, and a tuning circuit. The system architecture and its building blocks are chosen to minimize power consumption. Indeed, this sensor is designed to operate from harvested RF energy that provides very limited power. Therefore, reducing power consumption is a main priority of this project. To evaluate the performance of the proposed system, a behavioral model of the system was implemented with MATLAB/Simulink and the simulation results were reported. A feasibility check was done to better understand the power budget for the total system and for the main blocks of the system. Then, the main blocks were implemented and simulated using a 0.18 μm CMOS technology in the Cadence environment. An ultra-low power current reference was designed. It consumes only 31 nW.

The current reference circuit has three main points of interest: first, it has very low-power consumption. Second, it has a minimal number of branches - only two - and the latter has very low dependency on the temperature and supply voltage variations.

The current changes only by ±0.37% from its nominal value (16.2 nA) over temperatures ranging between -40 and 85 °C and the reference current variation in response to ±10% variation in the supply voltage is only ±0.14% from its nominal 16.2 nA value. Additionally, an ultra-low-power oscillator with low sensitivity to temperature variations was designed to generate a necessary clock signal. This oscillator is intended for ultra-low power and low-frequency applications. It consumes only 58 nW from a 1 V supply, while

occupying 190 µm x 120 µm of silicon area. In addition, it shows temperature sensitivity of ± 35 ppm/°C over temperatures ranging from -40 to 85 °C. The proposed structure has been designed and simulated with a 0.18 µm standard CMOS technology. The proper functionality of the presented design was validated through post-layout simulation results. The complete sensor comprises a tuning loop that consists of a peak detector, a comparator, a counter, and a binary to thermometer code conversion block.

4.2 Future work

There are a few promising avenues for future work:

- The assumed communication protocol that has been considered in this work is backscattering, but for better communication, a standard protocol such as Bluetooth Low Energy (BLE), ZigBee, and Wi-Fi could be used for communication.
- If higher accuracy for the sensor is needed, the accuracy could be increased via certain digital coding techniques.
- To obtain more compact wireless battery-less sensors, a tag antenna could be designed instead of a PCB-based antenna [82].
- Digital Optimization.

REFERENCES

[1] B. Razavi, *Design of analog CMOS integrated circuits*. Tata McGraw-Hill Education, 2002.

[2] P. Bergveld, "The impact of MOSFET-based sensors," *Sensors and Actuators*, vol. 8, no. 2, pp. 109–127, 1985, doi: https://doi.org/10.1016/0250-6874(85)87009-8.

[3] M. A. Fraga, H. Furlan, S. M. Wakavaiachi, and M. Massi, "Fabrication and characterization of piezoresistive strain sensors for high temperature applications," in *2010 IEEE International Conference on Industrial Technology*, 2010, pp. 513–516.

[4] Y. Koyamada, M. Imahama, K. Kubota, and K. Hogari, "Fiber-optic distributed strain and temperature sensing with very high measurand resolution over long range using coherent OTDR," *J. Light. Technol.*, vol. 27, no. 9, pp. 1142–1146, 2009.

[5] A. Davidson and C. Hill, "Measurement of building penetration into medium buildings at 900 and 1500 MHz," *IEEE Trans. Veh. Technol.*, vol. 46, no. 1, pp. 161–168, Feb. 1997, doi: 10.1109/25.554748.

[6] F. G. Osorio, M. Xinran, Y. Liu, P. Lusina, and E. Cretu, "Sensor network using power-over-ethernet," in *2015 International Conference and Workshop on Computing and Communication (IEMCON)*, 2015, pp. 1–7.

[7] I. Lobachev and E. Cretu, "Smart sensor network for smart buildings," in *2016 IEEE 7th Annual Information Technology, Electronics and Mobile Communication Conference (IEMCON)*, 2016, pp. 1–7.

[8] Y. Li, X. Cheng, Y. Cao, D. Wang, and L. Yang, "Smart choice for the smart grid: Narrowband Internet of Things (NB-IoT)," *IEEE Internet Things J.*, vol. 5, no. 3, pp. 1505–1515, 2017.

[9] Y. Qian, M. Tian, X. Jiang, H. Song, F. Shu, and J. Li, "Performance analysis for a two-way relaying power line network with analog network coding," *Front. Inf. Technol. Electron. Eng.*, vol. 16, no. 10, pp. 892–898, 2015.

[10] S. Güzelgöz, H. B. Çelebi, and H. Arslan, "Statistical characterization of the paths in multipath PLC channels," *IEEE Trans. power Deliv.*, vol. 26, no. 1, pp. 181–187, 2010.

[11] P. Popovski and H. Yomo, "Physical network coding in two-way wireless relay channels,"

in *2007 IEEE international conference on communications*, 2007, pp. 707–712.

[12] V. B. Balakirsky and A. J. H. Vinck, “Potential performance of PLC systems composed of several communication links,” in *International Symposium on Power Line Communications and Its Applications, 2005.*, 2005, pp. 12–16.

[13] H. Zou, A. Chowdhery, S. Jagannathan, J. M. Cioffi, and J. Le Masson, “Multi-user joint subchannel and power resource-allocation for powerline relay networks,” in *2009 IEEE International Conference on Communications*, 2009, pp. 1–5.

[14] Y. Qian *et al.*, “Design of hybrid wireless and power line sensor networks with dual-interface relay in IoT,” *IEEE Internet Things J.*, vol. 6, no. 1, pp. 239–249, 2017.

[15] T. R. Oliveira, C. A. G. Marques, M. S. Pereira, S. L. Netto, and M. V Ribeiro, “The characterization of hybrid PLC-wireless channels: A preliminary analysis,” in *2013 IEEE 17th International Symposium on Power Line Communications and Its Applications*, 2013, pp. 98–102.

[16] A. Mengi *et al.*, “IEEE 1905.1 hybrid home networking standard and its implementation with PLC, Wi-Fi and Ethernet technologies,” in *2016 International Symposium on Power Line Communications and its Applications (ISPLC)*, 2016, pp. 162–166.

[17] L. M. L. Oliveira, J. Reis, J. J. P. C. Rodrigues, and A. F. de Sousa, “IOT based solution for home power energy monitoring and actuating,” in *2015 IEEE 13th International Conference on Industrial Informatics (INDIN)*, 2015, pp. 988–992.

[18] A. Mckeown, H. Rashvand, T. Wilcox, and P. Thomas, “Priority SDN controlled integrated wireless and powerline wired for smart-home Internet of Things,” in *2015 IEEE 12th Intl Conf on Ubiquitous Intelligence and Computing and 2015 IEEE 12th Intl Conf on Autonomic and Trusted Computing and 2015 IEEE 15th Intl Conf on Scalable Computing and Communications and Its Associated Workshops (UIC-ATC-ScalCom)*, 2015, pp. 1825–1830.

[19] A. Dubey, R. K. Mallik, and R. Schober, “Performance analysis of a power line communication system employing selection combining in correlated log-normal channels and impulsive noise,” *IET Commun.*, vol. 8, no. 7, pp. 1072–1082, 2014.

[20] S. Galli, A. Scaglione, and Z. Wang, “For the grid and through the grid: The role of power line communications in the smart grid,” *Proc. IEEE*, vol. 99, no. 6, pp. 998–1027, 2011.

[21] L. Lampe and A. J. H. Vinck, “On cooperative coding for narrow band PLC networks,” *AEU-International J. Electron. Commun.*, vol. 65, no. 8, pp. 681–687, 2011.

[22] A. Shukla and S. Tripathi, “An effective relay node selection technique for energy efficient wsn-assisted iot,” *Wirel. Pers. Commun.*, vol. 112, no. 4, pp. 2611–2641, 2020.

[23] K. Akkaya and M. Younis, “A survey on routing protocols for wireless sensor networks,” *Ad hoc networks*, vol. 3, no. 3, pp. 325–349, 2005.

[24] X. Chen and N. C. Rowe, “An Energy-Efficient Communication Scheme in Wireless Cable Sensor Networks,” in *2011 IEEE International Conference on Communications (ICC)*, 2011, pp. 1–5.

[25] C.-T. Cheng, K. T. Chi, and F. C. M. Lau, “A delay-aware data collection network structure for wireless sensor networks,” *IEEE Sens. J.*, vol. 11, no. 3, pp. 699–710, 2010.

[26] J. Ko, C. Lu, M. B. Srivastava, J. A. Stankovic, A. Terzis, and M. Welsh, “Wireless sensor networks for healthcare,” *Proc. IEEE*, vol. 98, no. 11, pp. 1947–1960, 2010.

[27] M. reza Akhondi, A. Talevski, S. Carlsen, and S. Petersen, “Applications of wireless sensor networks in the oil, gas and resources industries,” in *2010 24th IEEE International Conference on Advanced Information Networking and Applications*, 2010, pp. 941–948.

[28] L. Ruiz-Garcia, L. Lunadei, P. Barreiro, and I. Robla, “A review of wireless sensor technologies and applications in agriculture and food industry: state of the art and current trends,” *sensors*, vol. 9, no. 6, pp. 4728–4750, 2009.

[29] G. Mois, S. Folea, and T. Sanislav, “Analysis of three IoT-based wireless sensors for environmental monitoring,” *IEEE Trans. Instrum. Meas.*, vol. 66, no. 8, pp. 2056–2064, 2017.

[30] D. B. Ashebo, C. A. Tan, J. Wang, and G. Li, “Feasibility of energy harvesting for powering wireless sensors in transportation infrastructure applications,” in *Proc.SPIE*, Apr. 2008, vol. 6934, doi: 10.1117/12.777866.

[31] J. Micek and J. Kapitulik, “Wireless sensors networks in road transportation applications,” in *Perspective Technologies and Methods in MEMS Design*, 2011, pp. 114–119.

[32] M. Tubaishat, P. Zhuang, Q. Qi, and Y. Shang, “Wireless sensor networks in intelligent transportation systems,” *Wirel. Commun. Mob. Comput.*, vol. 9, no. 3, pp. 287–302, 2009.

[33] H. C. Koydemir and A. Ozcan, “Wearable and Implantable Sensors for Biomedical Applications,” *Annu. Rev. Anal. Chem.*, vol. 11, no. 1, pp. 127–146, Jun. 2018, doi: 10.1146/annurev-anchem-061417-125956.

[34] M. A. Fonseca, M. G. Allen, J. Kroh, and J. White, “Flexible wireless passive pressure sensors for biomedical applications,” in *Tech. Dig. Solid-State Sensor, Actuator, and Microsystems Workshop (Hilton Head 2006)*, 2006, no. 1, pp. 37–42.

[35] S. Kanaparthi, V. R. Sekhar, and S. Badhulika, “Flexible, eco-friendly and highly sensitive paper antenna based electromechanical sensor for wireless human motion detection and structural health monitoring,” *Extrem. Mech. Lett.*, vol. 9, pp. 324–330, 2016, doi: https://doi.org/10.1016/j.eml.2016.09.007.

[36] N. Wang, N. Zhang, and M. Wang, “Wireless sensors in agriculture and food industry—Recent development and future perspective,” *Comput. Electron. Agric.*, vol. 50, no. 1, pp. 1–14, 2006.

[37] K. D. C. Stärk *et al.*, “Strengths and weaknesses of meat inspection as a contribution to animal health and welfare surveillance,” *Food Control*, vol. 39, pp. 154–162, 2014.

[38] K. K. Khedo, R. Perseedoss, and A. Mungur, “A wireless sensor network air pollution monitoring system,” *arXiv Prepr. arXiv1005.1737*, 2010.

[39] A. Kadri, E. Yaacoub, M. Mushtaha, and A. Abu-Dayya, “Wireless sensor network for real-time air pollution monitoring,” in *2013 1st international conference on communications, signal processing, and their applications (ICCSPA)*, 2013, pp. 1–5.

[40] Y. E. Aslan, I. Korpeoglu, and Ö. Ulusoy, “A framework for use of wireless sensor networks in forest fire detection and monitoring,” *Comput. Environ. Urban Syst.*, vol. 36, no. 6, pp. 614–625, 2012.

[41] J. S. Wilson, *Sensor technology handbook*. Elsevier, 2004.

[42] I. F. Akyildiz, W. Su, Y. Sankarasubramaniam, and E. Cayirci, "A survey on sensor networks," *IEEE Commun. Mag.*, vol. 40, no. 8, pp. 102–114, 2002.

[43] M. Minami, T. Morito, H. Morikawa, and T. Aoyama, "Solar biscuit: A battery-less wireless sensor network system for environmental monitoring applications," in *The 2nd international workshop on networked sensing systems*, 2005, vol. 2007.

[44] N. Zaman, L. Tang Jung, and M. M. Yasin, "Enhancing energy efficiency of wireless sensor network through the design of energy efficient routing protocol," *J. Sensors*, vol. 2016, 2016.

[45] J. M. Rabaey, M. J. Ammer, J. L. Da Silva, D. Patel, and S. Roundy, "PicoRadio supports ad hoc ultra-low power wireless networking," *Computer (Long. Beach. Calif).*, vol. 33, no. 7, pp. 42–48, 2000.

[46] J. Hill, R. Szewczyk, A. Woo, S. Hollar, D. Culler, and K. Pister, "System architecture directions for networked sensors," *ACM Sigplan Not.*, vol. 35, no. 11, pp. 93–104, 2000.

[47] X. Xu and H. Huang, "Battery-less wireless interrogation of microstrip patch antenna for strain sensing," *Smart Mater. Struct.*, vol. 21, no. 12, p. 125007, 2012.

[48] Q. Liu and Q.-J. Zhang, "Accuracy improvement of energy prediction for solar-energy-powered embedded systems," *IEEE Trans. Very Large Scale Integr. Syst.*, vol. 24, no. 6, pp. 2062–2074, 2015.

[49] C. Donovan, A. Dewan, D. Heo, and H. Beyenal, "Batteryless, wireless sensor powered by a sediment microbial fuel cell," *Environ. Sci. Technol.*, vol. 42, no. 22, pp. 8591–8596, 2008.

[50] S. M. Noghabaei, R. L. Radin, and M. Sawan, "Efficient Dual-band Ultra-Low-Power RF Energy Harvesting Front-End for Wearable Devices," in *2018 IEEE 61st International Midwest Symposium on Circuits and Systems (MWSCAS)*, 2018, pp. 444–447.

[51] X. Li, X. Meng, C.-Y. Tsui, and W.-H. Ki, "Reconfigurable resonant regulating rectifier with primary equalization for extended coupling-and loading-range in bio-implant wireless power transfer," *IEEE Trans. Biomed. Circuits Syst.*, vol. 9, no. 6, pp. 875–884, 2015.

[52] X. Li, C.-Y. Tsui, and W.-H. Ki, "A 13.56 MHz wireless power transfer system with reconfigurable resonant regulating rectifier and wireless power control for implantable medical devices," *IEEE J. Solid-State Circuits*, vol. 50, no. 4, pp. 978–989, 2015.

[53] J. Pan, A. A. Abidi, W. Jiang, and D. Marković, "Simultaneous transmission of up to 94-mW self-regulated wireless power and up to 5-Mb/s reverse data over a single pair of coils," *IEEE J. Solid-State Circuits*, vol. 54, no. 4, pp. 1003–1016, 2019.

[54] H. Lyu *et al.*, "Synchronized Biventricular Heart pacing in a closed-chest porcine Model based on Wirelessly powered Leadless pacemakers," *Sci. Rep.*, vol. 10, no. 1, pp. 1–9, 2020.

[55] H. Lyu and A. Babakhani, "A 13.56-MHz–25-dBm-Sensitivity Inductive Power Receiver System-on-a-Chip with a Self-Adaptive Successive Approximation Resonance Compensation Front-End for Ultra-Low-Power Medical Implants," *IEEE Trans. Biomed. Circuits Syst.*, 2020.

[56] A. Agarwal *et al.*, "A 4μW, ADPLL-based implantable amperometric biosensor in 65nm CMOS," in *2017 Symposium on VLSI Circuits*, 2017, pp. C108–C109.

[57] R. Muller *et al.*, "A minimally invasive 64-channel wireless μECoG implant," *IEEE J. Solid-State Circuits*, vol. 50, no. 1, pp. 344–359, 2014.

[58] Y.-J. Huang *et al.*, "A self-powered CMOS reconfigurable multi-sensor SoC for biomedical applications," *IEEE J. Solid-State Circuits*, vol. 49, no. 4, pp. 851–866, 2014.

[59] S.-Y. Lee *et al.*, "A programmable implantable microstimulator SoC with wireless telemetry: Application in closed-loop endocardial stimulation for cardiac pacemaker," *IEEE Trans. Biomed. Circuits Syst.*, vol. 5, no. 6, pp. 511–522, 2011.

[60] P. Cong, N. Chaimanonart, W. H. Ko, and D. J. Young, "A wireless and batteryless 10-bit implantable blood pressure sensing microsystem with adaptive RF powering for real-time laboratory mice monitoring," *IEEE J. Solid-State Circuits*, vol. 44, no. 12, pp. 3631–3644, 2009.

[61] K. J. Cho and H. H. Asada, "Wireless, battery-less stethoscope for wearable health monitoring," in *Proceedings of the IEEE 28th Annual Northeast Bioengineering Conference (IEEE Cat. No. 02CH37342)*, 2002, pp. 187–188.

[62] N. Verma and A. P. Chandrakasan, “A 25/spl mu/W 100kS/s 12b ADC for wireless micro-sensor applications,” in *2006 IEEE International Solid State Circuits Conference-Digest of Technical Papers*, 2006, pp. 822–831.

[63] N. Verma and A. P. Chandrakasan, “An ultra low energy 12-bit rate-resolution scalable SAR ADC for wireless sensor nodes,” *IEEE J. Solid-State Circuits*, vol. 42, no. 6, pp. 1196–1205, 2007.

[64] M. Cai, K. Takahata, and S. Mirabbasi, “A Low-Voltage Low-Power Implantable Telemonitoring System with Application to Endo-Hyperthermia Treatment of In-Stent Restenosis,” in *2020 18th IEEE International New Circuits and Systems Conference (NEWCAS)*, 2020, pp. 331–334.

[65] E. Y. Chow, A. L. Chlebowski, S. Chakraborty, W. J. Chappell, and P. P. Irazoqui, “Fully wireless implantable cardiovascular pressure monitor integrated with a medical stent,” *IEEE Trans. Biomed. Eng.*, vol. 57, no. 6, pp. 1487–1496, 2010.

[66] M. Salehi, M. Ali, Y. Savaria, and M. Sawan, “A 58 nW±35 ppm/° C Oscillator for IoT Battery-less Sensor Applications,” in *2020 27th IEEE International Conference on Electronics, Circuits and Systems (ICECS)*, 2020, pp. 1–4.

[67] A. Joshi and R. Singhal, “Coaxially Fed Hexagonal Patch Antenna for C-and X-band Applications with Reduced-Ground Plane,” *ECTI Trans. Electr. Eng. Electron. Commun.*, vol. 17, no. 2, pp. 136–143, 2019.

[68] S. Kim *et al.*, “Ambient RF energy-harvesting technologies for self-sustainable standalone wireless sensor platforms,” *Proc. IEEE*, vol. 102, no. 11, pp. 1649–1666, 2014.

[69] B. Li, X. Shao, N. Shahshahan, N. Goldsman, T. Salter, and G. M. Metze, “An antenna co-design dual band RF energy harvester,” *IEEE Trans. Circuits Syst. I Regul. Pap.*, vol. 60, no. 12, pp. 3256–3266, 2013.

[70] Z. Hameed and K. Moez, “A 3.2 V–15 dBm adaptive threshold-voltage compensated RF energy harvester in 130 nm CMOS,” *IEEE Trans. Circuits Syst. I Regul. Pap.*, vol. 62, no. 4, pp. 948–956, 2015.

[71] S. S. Hashemi, M. Sawan, and Y. Savaria, “A high-efficiency low-voltage CMOS rectifier

for harvesting energy in implantable devices," *IEEE Trans. Biomed. Circuits Syst.*, vol. 6, no. 4, pp. 326–335, 2012.

[72] M. K. Amaljith, G. H. Rao, and S. Rekha, "Low voltage current reference circuit with low temperature coefficient," in *2018 IEEE Distributed Computing, VLSI, Electrical Circuits and Robotics (DISCOVER)*, 2018, pp. 60–63.

[73] V. Jahagirdar and R. Hirur, "CMOS current reference with temperature compensation," in *2015 IEEE International Conference on Electrical, Computer and Communication Technologies (ICECCT)*, 2015, pp. 1–4.

[74] K. Tsubaki, T. Hirose, N. Kuroki, and M. Numa, "A 32.55-kHz, 472-nW, 120ppm/° C, fully on-chip, variation tolerant CMOS relaxation oscillator for a real-time clock application," in *2013 Proceedings of the ESSCIRC (ESSCIRC)*, 2013, pp. 315–318.

[75] T. Tokairin *et al.*, "A 280nW, 100kHz, 1-cycle start-up time, on-chip CMOS relaxation oscillator employing a feedforward period control scheme," in *2012 Symposium on VLSI Circuits (VLSIC)*, 2012, pp. 16–17.

[76] H. Wang and P. P. Mercier, "A reference-free capacitive-discharging oscillator architecture consuming 44.4 pW/75.6 nW at 2.8 Hz/6.4 kHz," *IEEE J. Solid-State Circuits*, vol. 51, no. 6, pp. 1423–1435, 2016.

[77] D. A. Johns and K. Martin, *Analog integrated circuit design*. John Wiley & Sons, 2008.

[78] R. J. Baker, *CMOS: circuit design, layout, and simulation*. John Wiley & Sons, 2019.

[79] R. Katreepalli and T. Haniotakis, "Power efficient synchronous counter design," *Comput. Electr. Eng.*, vol. 75, pp. 288–300, 2019.

[80] G. Bertotti *et al.*, "An 8 bit current steering DAC for offset compensation purposes in sensor arrays," *Adv. Radio Sci.*, vol. 10, no. D. 3, pp. 201–206, 2012.

[81] B. Razavi, "The StrongARM latch [a circuit for all seasons]," *IEEE Solid-State Circuits Mag.*, vol. 7, no. 2, pp. 12–17, 2015.

[82] M. T. Islam, T. Alam, I. Yahya, and M. Cho, "Flexible radio-frequency identification (RFID) tag antenna for sensor applications," *Sensors*, vol. 18, no. 12, p. 4212, 2018.

[83] T. Hirose, Y. Osaki, N. Kuroki, and M. Numa, “A nano-ampere current reference circuit and its temperature dependence control by using temperature characteristics of carrier mobilities,” in *2010 Proceedings of ESSCIRC*, 2010, pp. 114–117.

[84] M. A. C. Aguinaga *et al.*, “Development of an ultra-low power current reference circuit for passive RFID application in 90nm CMOS technology,” in *TENCON 2017-2017 IEEE Region 10 Conference*, 2017, pp. 2789–2794.

[85] R. Carvalho *et al.*, “A Low-Power CMOS Current Reference for Piezoelectric Energy Harvesters,” *IEEE Trans. Electron Devices*, vol. 67, no. 8, pp. 3403–3410, 2020.

[86] M. S. Eslampanah, S. Kananian, E. Zendehrouh, M. Sharifkhani, A. M. Sodagar, and M. Shabany, “A low-power temperature-compensated CMOS peaking current reference in subthreshold region,” in *2017 IEEE International Symposium on Circuits and Systems (ISCAS)*, 2017, pp. 1–4.

[87] G. De Vita, F. Marraccini, and G. Iannaccone, “Low-voltage low-power CMOS oscillator with low temperature and process sensitivity,” in *2007 IEEE International Symposium on Circuits and Systems*, 2007, pp. 2152–2155.

[88] J. Wang, L. H. Koh, and W. L. Goh, “A 13.8-MHz RC oscillator with self-calibration for±0.4% temperature stability from− 55 to 125° C,” in *2015 IEEE International Conference on Electron Devices and Solid-State Circuits (EDSSC)*, 2015, pp. 423–426.

[89] Y. Ni and M. Onabajo, “A low-power temperature-compensated CMOS relaxation oscillator,” *Analog Integr. Circuits Signal Process.*, vol. 79, no. 2, pp. 309–317, 2014.

[90] L. Xu and M. Onabajo, “A low-power temperature-compensated relaxation oscillator for built-in test signal generation,” in *2015 IEEE 58th international midwest symposium on circuits and systems (MWSCAS)*, 2015, pp. 1–4.